CHEMISTRY
A European Journal

A Journal of
ChemPubSoc Europe

Accepted Article

Title: Strong Influence of the Ancillary Ligand over the Photodynamic Anticancer Properties of Neutral Biscyclometalated Ir(III) Complexes Bearing 2-Benzoazole-Phenolates

Authors: Marta Martínez-Alonso, Natalia Busto, Larry Danilo Aguirre, Leticia Berlanga, María del Carmen Carrión, José Vicente Cuevas, Ana María Rodríguez, Arancha Carbayo, Blanca Rosa Manzano, Enrique Ortí, Félix Ángel Jalón, Begoña García, and Gustavo Espino

To be cited as: *Chem. Eur. J.* 10.1002/chem.201803784

Link to VoR: http://dx.doi.org/10.1002/chem.201803784

Supported by
ACES

WILEY-VCH

10.1002/chem.201803784

Strong Influence of the Ancillary Ligand over the Photodynamic Anticancer Properties of Neutral Biscyclometalated Ir(III) Complexes Bearing 2-Benzoazole-Phenolates

Marta Martínez-Alonso,[$,a] Natalia Busto,[$,a] Larry Danilo Aguirre,[d] Leticia Berlanga,[a] M. Carmen Carrión,[b] José V. Cuevas,[a] Ana M. Rodríguez,[b] Arancha Carbayo,[a] Blanca R. Manzano,[b] Enrique Ortí,[c] Félix A. Jalón,[b] Begoña García,*[a] and Gustavo Espino*[a]

[$] These authors contributed equally to the work.

[a]*Departamento de Química, Facultad de Ciencias, Universidad de Burgos, Plaza Misael Bañuelos s/n, 09001, Burgos, Spain.*

[b]*Departamento de Química Inorgánica, Orgánica y Bioquímica, Facultad de Químicas, Universidad de Castilla-La Mancha, Avda. Camilo J. Cela 10, 13071 Ciudad Real, Spain.*

[c]*Instituto de Ciencia Molecular, Universidad de Valencia, Catedrático José Beltrán 2, 46980 Paterna, Spain.*

[d]*Facultad de Ingeniería Eléctrica y Electrónica. Universidad Nacional de Ingeniería. Av. Túpac Amaru 210, PE-LIMA 025, Lima, Perú.*

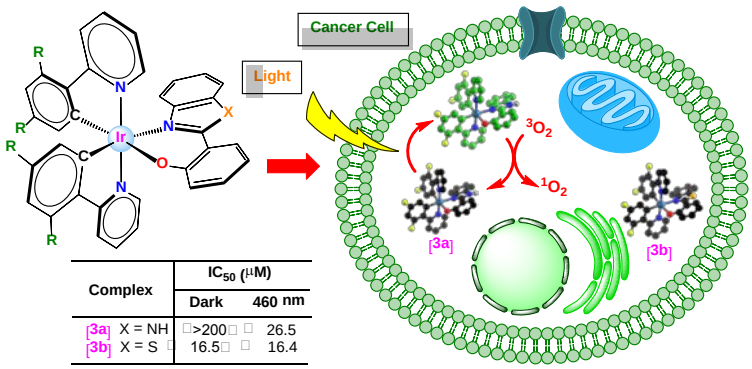

Complex		IC_{50} (μM) Dark	IC_{50} (μM) 460 nm
[3a]	X = NH	>200	26.5
[3b]	X = S	16.5	16.4

Keywords: Heteroleptic neutral Iridium(III) complexes / 2-arylazoles / phosphorescent complexes / Photodynamic therapy / Anticancer complexes.

ABSTRACT

In this paper we describe the synthesis, comprehensive characterization and biological and photocatalytic properties of two series of neutral Ir(III) biscyclometalated complexes of general formula [Ir(C^N)$_2$(N^O)], where the N^O ligands are 2-(benzimidazolyl)phenolate-*N,O* (**L1**, ***series a***) and 2-(benzothiazolyl)phenolate-*N,O* (**L2**, **series b**), and the C^N ligands are 2-(phenyl)pyridinate or its derivatives. Complexes of types **a** and **b** exhibit dissimilar photophysical and biological properties. *In vitro* cytotoxicity tests conclusively prove that

derivatives of **series a** are harmless in the dark against SW480 cancer cells (colon adenocarcinoma), but express enhanced cytotoxicity versus the same cells after stimulation with UV or blue light. In contrast, complexes of type **b** show a very high cytotoxic activity in the dark, but low photosensitizing ability. Thus, the ancillary N^O ligand is the main factor in terms of cytotoxic activity both in the dark and upon irradiation. However, the C^N ligands play a key role regarding metal accumulation in cells. In particular, the complex of formula [Ir(dfppy)$_2$(**L1**)] (dfppy = 2-(4,6-difluorophenyl)pyridinate) [**3a**] has been identified as both an efficient photosensitizer for $^1O_2$ generation and a potential agent for photodynamic therapy. These capabilities are probably related to a combination of its notable cellular internalization, remarkable photostability, high photoluminescence quantum yield, and long triplet excited-state lifetime. Both types of complexes exhibit notable catalytic activity in the photooxidation of thioanisole and S-containing aminoacids with full selectivity.

INTRODUCTION

Light-mediated therapy or phototherapy (PT) is a clinically approved, minimally invasive chemotherapeutic protocol that can exert a very selective and controlled cytotoxic activity toward malignant cells. PT involves the administration of a photosensitizing chemical agent (photosensitizer, PS) which ideally shows negligible cytotoxicity in the absence of light. Subsequently, the PS is excited by irradiation with light to initiate a photochemical reaction that produces biologically active species at cytotoxic levels, which are able to damage cell bio-targets and lead to cell death via apoptosis or necrosis.[1] Two types PT protocols or treatments are known depending on the mechanism of action of the specific PS:[2,3]

(a) O_2-dependent treatments, where the PS exerts its action by producing highly reactive oxygen species (ROS) from cellular O_2. This kind of protocol is called photodynamic therapy (PDT) and is classified into type I processes when the PS produces oxygen radicals and other ROS through an electron transfer reaction, and type II when the PS generates the very reactive $^1O_2$ from ground state $^3O_2$ through an energy transfer process.[4]

(b) O_2-independent treatments, where the PS performs its biological activity either through direct electron transfer reactions from the excited state of the PS to cellular targets, or alternatively, through photoinduced dissociation/release of ligands/drugs from metal complexes or organic caging groups. The latter strategy is called photoactivated chemotherapy (PACT) and gives rise to chemotherapeutic agents with potential dual activity when both the free ligand and the metal fragment or organic caging exhibit cytotoxic action.[5,6]

In particular, the more conventional O_2-dependent type II-PDT strategy involves the combination of three essential and separately non-toxic components: a photochemically active drug (PS), light of suitable wavelength, and the O_2 dissolved in the tissues.[7]

Useful light in PDT must combine two requirements: efficiency in penetration of tissues and high ability in $^1O_2$ generation. On the one hand, red and infrared lights penetrate more deeply through tissues than blue light and the region between 600 and 1200 nm is often called the optical window of tissue. On the other hand, wavelengths longer than 800 nm cannot generate $^1O_2$, since they have insufficient energy to initiate a photodynamic reaction.[8]

Approved PDT agents are macrocyclic organic molecules (porphyrin-, phtalocyanine- and chlorin-based derivatives) that photo-induce the generation of $^1O_2$ or ROS. Nevertheless, these PSs often suffer from different drawbacks, such as laborious synthetic and purification protocols, troublesome chemical modification, low water solubility, absence of light absorptions in the ideal wavelength range (*vide infra*) (e.g., Photofrin),[9] low efficiency under low O_2

concentrations,[10] and slow excretion that give rise to prolonged photosensitivity in the patients.[11]

The ideal attributes desirable for an efficient photosensitizer (PS) for singlet oxygen ($^1O_2$) generation in the context of PDT are:[9,12,13] (1) strong light absorption ability, particularly in the wavelength range between 650 and 800 nm so that they can take advantage of the deeper tissue penetration of red light and infrared radiation, (2) high intersystem crossing efficiency, which favors high quantum yields in the formation of the PS triplet excited state, and consequently in the generation of $^1O_2$ or ROS in water, (3) long PS triplet excited state lifetimes that make the bimolecular collision with $^3O_2$ more probable, (4) an energy gap between the triplet excited state (T_1) and the singlet ground state (S_0) that exceeds the excitation energy to produce $^1O_2$ from $^3O_2$ (the latter being 1268 nm = 0.98 eV), (5) low quenching rate of $^1O_2$, since many $^1O_2$ photosensitizers can also efficiently deactivate $^1O_2$ to $^3O_2$, (6) good solubility and stability in physiological media and amphiphilic character to ensure cellular uptake, (7) selective accumulation in the cancer cells, negligible cytotoxicity in the dark, and non-mutagenic nature, (8) good photostability and stability against photooxidation by $^1O_2$ to prevent degradation and loss of sensitizing ability, and finally (9) rapid excretion from the body.

In general, phosphorescent biscyclometalated iridium(III) complexes display very interesting emission properties, e.g., high quantum yields, large Stokes shifts, long-lived phosphorescence, modular color-tuning possibilities, and good photostability. As a result, they are being studied in the development of solid-state lighting devices, such as organic light-emitting diodes (OLEDs)[14] and light-emitting electrochemical cells (LECs),[15,16] as biological imaging agents,[17] and as analytical probes.[18] In addition, they work as efficient PSs in singlet oxygen production and can be used as O_2 probes,[19,20] as photodynamic anticancer agents,[21–30][31–33][34] and as catalysts in photooxidation reactions.[35] Previous reports have shown that biscyclometalated Ir(III) complexes with 2-(2-hydroxyphenyl)oxazole-based N^O ancillary ligands, similar to those used in this work, exhibit highly efficient phosphorescence.[36]

With these precedents in mind, in this work we aimed to synthesize two series of neutral Ir(III) biscyclometalated complexes of general formula [Ir(C^N)$_2$(N^O)], where the N^O ligands are 2-(benzimidazolyl)phenolate-*N,O* (**series a**) and 2-(benzothiazolyl)phenolate-*N,O* (**series b**), and to assess their photophysical and anticancer properties and in particular their potential as PDT agents. An additional goal was to test their catalytic behavior in the photooxydation of thioanisol and S-containing aminoacids.

RESULTS AND DISCUSSION

Synthesis and Characterization

The synthetic method and the molecular structures of the neutral complexes described herein are sketched in Scheme 1. The [Ir(C^N)$_2$(N^O)] complexes (C^N = 2-(phenyl)pyridinato-C^2,*N* (*ppy*), 2-(4-tolyl)pyridinato-C^2,*N* (*tolpy*), and 2-(4,6-difluorophenyl)pyridinato-C^2,*N* (*dfppy*); N^O = 2-(benzimidazolyl)phenolate-*N,O* (**L1**) and 2-(benzothiazolyl)phenolate-*N,O* (**L2**)) were prepared in two steps. In the first step the chloro-bridged dimeric iridium(III) complexes *rac*-[Ir(C^N)$_2$(μ-Cl)]$_2$ (C^N = *ppy*, *tolpy*) were obtained by reacting $IrCl_3$ hydrate and 2-phenylpyridine (*ppy*-H) or 2-(*p*-tolyl)pyridine (*tolpy*-H) in 2-ethoxyethanol/water (3:1 v/v) under reflux according to the well-established protocols reported in the literature.[37,38] The *rac*-[Ir(C^N)$_2$(μ-Cl)]$_2$ dimer with C^N = *dfppy* was prepared more efficiently by an adapted procedure using a microwave heating source. Then, the isolated dimeric starting materials were reacted with the corresponding pro-ligands **HL1** and **HL2** in the presence of Na_2CO_3 under refluxing 2-ethoxyethanol/water. Complex [**1b**] has been previously described by Li et al. and proposed as a phosphorescent Hg^{2+}-selective chemodosimeter.[39]

10.1002/chem.201803784

The new compounds exhibit C_1 molecular symmetry and helicoidal chirality due to the presence of three bis(chelate) ligands and so they were isolated as racemic mixtures (Δ,Λ) of yellow ([**1a**]–[**3a**]) to red-orange ([**1b**]–[**3b**]) solids in good yields and with good purity. The complexes are soluble in dimethylsulfoxide and other organic solvents, but insoluble in water.

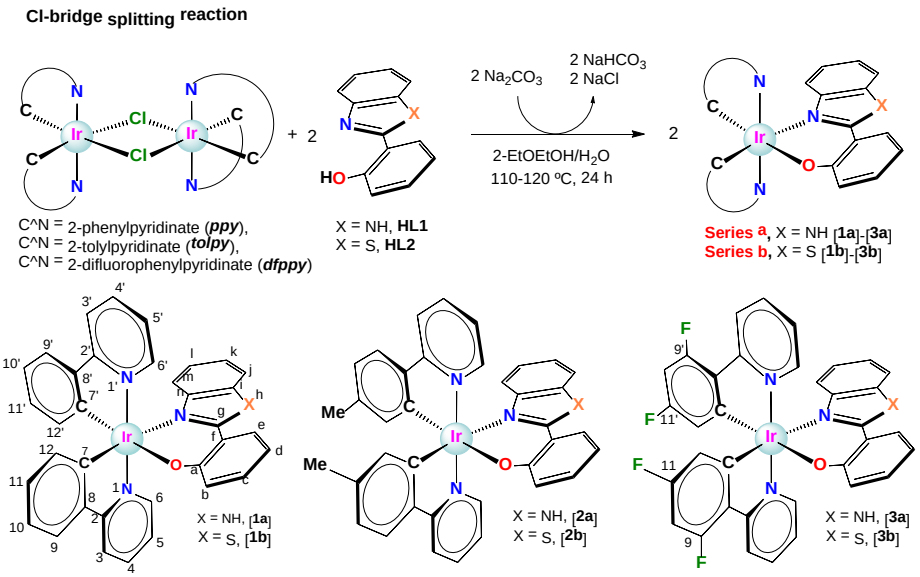

Scheme 1. Synthesis and molecular structures of the neutral complexes [**1a**]–[**3a**] and [**1b**]–[**3b**], showing atom numbering scheme, abbreviations, and labels used throughout the whole text. Only Λ enantiomers are shown.

The composition and molecular structure of all the complexes were determined by multinuclear NMR, IR, mass spectroscopy, and elemental analysis. Two-dimensional NMR experiments were used to identify the signals of all the nuclei in the ^{1}H and ^{13}C{^{1}H} NMR spectra.

The ^{1}H, ^{13}C{^{1}H}, and ^{19}F NMR spectra of the new complexes exhibit one set of peaks for each of the two inequivalent C^N ligands due to the asymmetric nature of the coordination environment around the metal. For instance, the ^{1}H NMR spectra of complexes [**2a**] and [**2b**] display two singlets each, for the Me groups of *tolpy*, whilst the ^{19}F NMR spectra of complexes [**3a**] and [**3b**] show two quartets, each corresponding to atoms labeled as F^{11} and $F^{11'}$, and two triplets, each assigned to atoms F^{9} and $F^{9'}$ of *dfppy* (Figure S1). The unequivocal assignation of all the signals in the ^{1}H NMR and ^{19}F NMR of some derivatives was possible owing to the observation of crucial interligand NOE cross peaks $H^{6}\leftrightarrow H^{12'}\leftrightarrow H^{m}\leftrightarrow H^{6}$ and $H^{6'}\leftrightarrow H^{12}$, as well as interring NOE cross peaks $H^{3}\leftrightarrow H^{9}$, $H^{3'}\leftrightarrow H^{9'}$, $H^{3}\leftrightarrow F^{9}$ and $H^{3'}\leftrightarrow F^{9'}$ in the 2D NOESY and ^{19}F-^{1}H HOESY spectra (see Figures S2 and S3). Additional features in the spectra of the new derivatives confirm the expected structures: (a) broad singlets around 13 ppm for the N−H protons of complexes [**1a**], [**2a**], and [**3a**]; (b) the shifting of the signals for the ancillary anionic ligands **L1** and **L2** with regard to the respective resonances of the protonated pro-ligands **HL1** and **HL2**, and (c) the absence of peaks for O−H groups.

The FAB+ mass spectra of the six complexes show envelope peaks whose m/z ratio and isotopic distribution are compatible with the $[M+H]^{+}$ or $[M]^{+}$ cations. In addition, the $[Ir(C\text{^}N)_2]^{+}$ fragments are observed in all the spectra, confirming that the N^O ligands are more labile than the corresponding cyclometalated ligands.

10.1002/chem.201803784

Crystal Structure by X-ray Diffraction

The crystal structure of [**1b**] has been previously reported.[39] Single crystals of [**3a**]**x 0.25 Me_2CO** suitable for X-ray diffraction analysis were obtained by slow diffusion of acetone into a methanol solution of this complex. [**3a**] crystallizes in the monoclinic space group $P2_1/c$ with 0.25 molecules of acetone. The ORTEP diagram for the asymmetric unit is depicted in Figure 1, whereas selected bond lengths and angles with estimated standard deviations are gathered in Table S1, and crystallographic refinement parameters are given in Table S2. The corresponding unit cell shows two pairs of the enantiomers (Λ and Δ). The iridium center displays a slightly distorted octahedral coordination geometry with the expected *cis*-C,C and *trans*-N,N mutual disposition for the *dfppy* ligands.[40] The Ir−C_{dfppy} and Ir−N_{dfppy} bond distances lie in the expected range typical of phenylpyridinate type ligands (very close to 2 Å).[41–46] The bond lengths for the ancillary ligand are significantly longer due to the strong *trans* influence exerted by the donor C atoms, Ir(1)−N(1) = 2.147(4) Å and Ir(1)−O(1) = 2.159(3) Å.[47,48] The bite angle for **L1**, N(1)−Ir(1)−O(1) = 84.0(1)º, is comparable to those previously reported for six-membered N−Ir−O iridacycles in analogous derivatives,[39] and the C−Ir−N bite angles for the cyclometalated C^N ligands, C(35)−Ir(1)−N(4) and C(24)−Ir(1)-N(3), are also standard (~80º).[49,50]

In the molecular structure of **[3a]** the H···H interligand distances ($H^6 \leftrightarrow H^{12'} \leftrightarrow H^m \leftrightarrow H^6$ and $H^{6'} \leftrightarrow H^{12}$, see Scheme 1 for numbering and Figure S4) are shorter than 3.7 Å. These measurements are in agreement with the observed NOE interactions in the 2D NOESY spectra, which have been used for the complete assignment of the ^{1}H NMR resonances.

The 3D crystal packing is stabilized by intermolecular hydrogen bonds, (N(2)−H(2A)···O(1) and C(9)−H(9)···F(3)), CH–π contacts and offset π–π stacking interactions between pairs of difluorophenyl and hydroxophenyl rings (see Tables S3-S5 and Figure S5). It is interesting to note that the same phenoxy ring exhibits a CH–π contact on one side and a π–π stacking interaction on the opposite site reflecting a possible synergistic effect as it has been previously reported from ab initio calculations.[51]

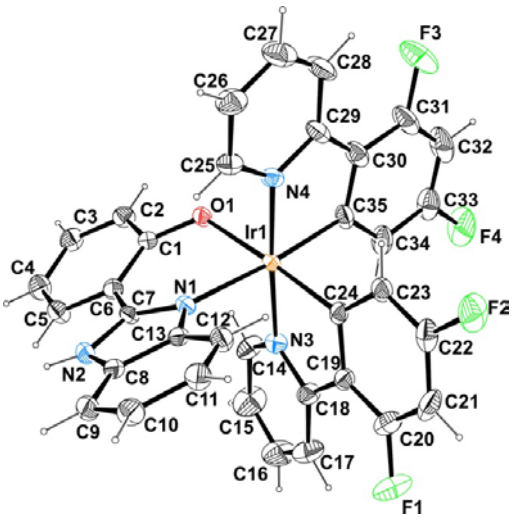

Figure 1. ORTEP diagram for (Δ)-**[3a]** forming the asymmetric unit of racemic **[3a]**. Thermal ellipsoids are shown at the 30% probability level. Selected bond lengths (Å) for the coordination polyhedron of **[3a]** are: Ir(1)−C(24) = 1.989(5); Ir(1)−C(35) = 2.002(5); Ir(1)−N(3) = 2.035(4); Ir(1)−N(4) = 2.036(4); Ir(1)−N(1) = 2.147(4); Ir(1)−O(1) = 2.159(3).

10.1002/chem.201803784

Electrochemical properties

The redox potentials of complexes [**1a**]–[**3a**] and [**1b**]–[**3b**] were experimentally measured in acetonitrile solutions (3×10^{-4} M) by cyclic voltammetry using [^{n}Bu$_4$N][PF$_6$] (0.1 M) as supporting electrolyte and glassy carbon as working electrode. Argon was bubbled through the solutions to displace oxygen. Potentials were referred to the ferrocene/ferrocenium (Fc/Fc$^+$) couple. The anodic region of the corresponding voltammograms show irreversible or quasi-reversible oxidation peaks between +0.45 and +0.83 V (see Table 1 and Figure 2), which are ascribed to the oxidation of the Ir(III)-phenoxy entities as discussed in depth below. Notably, small effects on the potential values are attributed to both the N^O and C^N ligands.

The interpretation of the cathodic region provided the following trends: (a) all the compounds with ligand **L1** (X = N−H) exhibit a totally irreversible weak peak between –2.30 and –2.40 V, in agreement with the instability of the respective reduced species (Figure S6); (b) another quasi-reversible peak is observed at –2.64, –2.70, and –2.46 V for compounds [**1a**], [**2a**], and [**3a**], respectively; (c) as for complexes of type **b**, they exhibit a single quasi-reversible reduction peak at lower potentials (–2.27, –2.17, and –2.11 V) compared to their relatives of type **a**, in agreement with the stabilization of the lowest-unoccupied molecular orbital (LUMO) for type **b** derivatives as discussed below; (d) the *dfppy* cyclometalated ligand shifts significantly the reduction peaks to less cathodic potentials.

Table 1. Cyclic voltammetric data referenced to Fc/Fc$^+$ in acetonitrile solution (3×10^{-4} M)[a]

Compound	$E^{ox}_{1/2}$ (V)	$E^{red}_{1/2}$ (V)	$\Delta E_{1/2}$ (V)[b]
[**1a**]	0.45 (qr)	–2.64 (qr)	3.09
[**1b**]	0.58 (ir)	–2.27 (qr)	2.85
[**2a**]	0.45 (qr)	–2.70 (qr)	3.15
[**2b**]	0.63 (qr)	–2.17 (qr)	2.80
[**3a**]	0.63 (ir)	–2.46 (qr)	3.09
[**3b**]	0.83 (ir)	–2.11 (qr)	2.94

[a] Measured using [^{n}Bu$_4$N][PF$_6$] (0.1 M) as supporting electrolyte and a scan rate of 0.1 V s^{-1} (qr = quasi-reversible, ir = irreversible). $\Delta E_{1/2} = E^{ox}_{1/2} - E^{red}_{1/2}$.

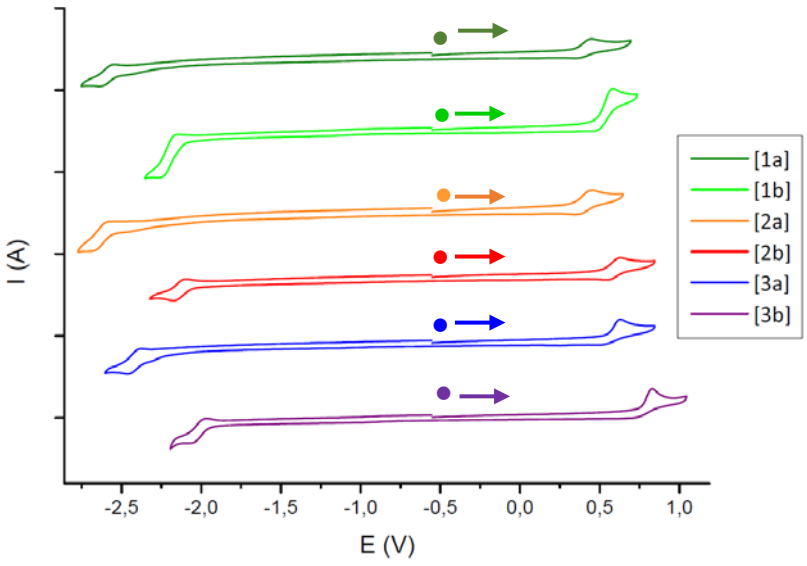

Figure 2. (a) Cyclic voltammograms of complexes [**1a**]–[**3b**] in acetonitrile solution (3×10^{-4} M), using [^{n}Bu$_4$N][PF$_6$] (0.1 M) as supporting electrolyte. Scan rate of 0.1 V s^{-1}. (•) Indicates the starting (E_i) and final potential (E_f), $E_i = E_f = -0.55$ V (vs. Fc/Fc$^+$), clockwise scan.

10.1002/chem.201803784

Photophysical properties

Electronic absorption properties. The UV-vis absorption spectra and the absorption maxima data recorded for complexes [**1a**]–[**3a**] and [**1b**]–[**3b**] in deoxygenated acetonitrile (10^{-5} M) at 25 ºC are shown in Figure 3 and Table 2, respectively. All the complexes exhibit intense ($\varepsilon >$ 40000 $M^{-1}\cdot cm^{-1}$) and broad absorption bands in the ultraviolet region below 300 nm, attributed to spin-allowed intraligand transitions (^{1}IL) ($\pi \rightarrow \pi^*$) within the cyclometalated (N^C) and ancillary (N^O) ligands. The less intense absorption bands and shoulders recorded at $\lambda >$ 350 nm and weak absorptions extending into the visible region are assigned to spin-allowed singlet-to-singlet metal-to-ligand charge transfer (^{1}MLCT) transitions and spin-forbidden singlet-to-triplet ^{3}MLCT (d_π(Ir) $\rightarrow \pi^*$(N^C and N^O)) transitions, as well as spin-forbidden ligand-to-ligand charge transfer (^{3}LLCT) ($\pi_{N\text{^}O} \rightarrow \pi^*_{C\text{^}N}$) and ligand-centered (^{3}LC) ($\pi \rightarrow \pi^*$) transitions.[52–56] Apart from the above-mentioned features common to all the complexes, some differences are found in the absorption spectra of these derivatives depending on the ancillary ligand. In particular, complexes [**1a**]–[**3a**] bearing **L1** show relative maxima in the 350–390 nm range ($9240 < \varepsilon < 11270$ $M^{-1}\cdot cm^{-1}$) and then a weak absorption between 430 and 500 nm, whereas complexes [**1b**]–[**3b**] with **L2** lack the relative maxima in the 350–390 nm range but display a more intense absorption above 425 nm that introduces itself well into the visible (λ = 450 nm with $\varepsilon >$ 6000 $M^{-1}\cdot cm^{-1}$).

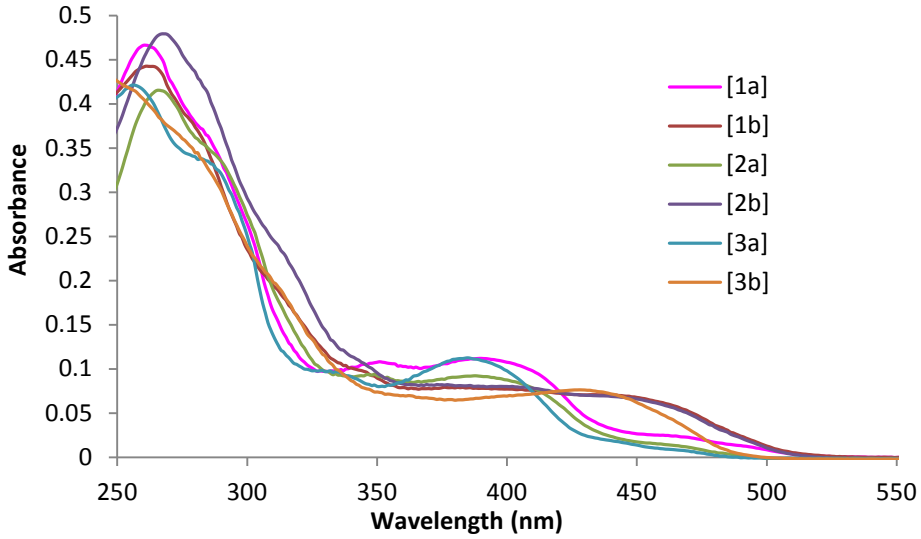

Figure 3. Overlaid UV-Vis absorption spectra of complexes **[1a]–[3a]** and **[1b]–[3b]** in deoxygenated acetonitrile (10^{-5} M) at 25 °C.

Table 2. Wavelengths (λ_{abs}/nm) and molar extinction coefficients (ε/$M^{-1}\cdot cm^{-1}$) at the absorption maxima in the UV-Vis spectra of complexes [**1a**]–[**3a**] and [**1b**]–[**3b**] measured in deoxygenated acetonitrile (10^{-5} M) at 25 °C.

[1a]		[1b]		[2a]		[2b]		[3a]		[3b]	
λ_{abs}	ε	λ_{abs}	ε	λ_{abs}	ε	λ_{abs}	ε	λ_{abs}	ε	λ_{abs}	ε
261	46640	261	44270	266	41550	268	47930	256	42140	250	42580
351	10830	-	-	349	9410	-	-	334	9710	-	-
390	11210	-	-	388	9240	-	-	385	11270	-	-
450[a]	2670	450[a]	6790	450[a]	1760	450[a]	6610	450[a]	1400	450[a]	6210

[a] These wavelengths do not correspond to relative maxima but allow to compare the absorption at 450 nm.

In addition, the UV-Vis absorption spectra of the Ir complexes (Figure S7) were recorded under the conditions used for the *in cellulo* studies (*vide infra*). Table S6 shows the respective molar

10.1002/chem.201803784

extinction coefficients recorded at the irradiation wavelengths used in the photo-cytotoxicity experiments, i.e.: UV (365 nm) and blue (460 nm). All the complexes bearing **L2** as ancillary ligand display higher absorptivity in the blue light irradiation wavelenght (460 nm) than the complexes of series **a**, whereas absorptivity in UV light irradiation wavelength (365nm) cannot be used to differentiate between both series.

Photoluminescence properties. The complexes with **L1** exhibit green photoluminescence, whereas those complexes with **L2** glow with orange light under UV radiation. The emission spectra of complexes [**1a**]–[**3a**] and [**1b**]–[**3b**] upon excitation at the respective wavelengths in deoxygenated acetonitrile at room temperature are shown in Figure 4 and the photophysical data are compiled in Table 3. In these conditions, all the complexes display broad emission bands, with emission maxima appearing in the range between 512 and 533 nm for [**1a**]–[**3a**], and between 580 and 607 nm for [**1b**]–[**3b**]. Hence, there is a strong dependence of the emission energy on the N^O ligand, the red shift observed on replacing **L1** with **L2** being tentatively explained as due to the lower electron-donor ability of the benzothiazole moiety in **L2** compared with the benzimidazole unit in **L1**.[16] As discussed below, this leads to the stabilization of the LUMO and consequently to the reduction of the energy gap. In contrast, the effect of the C^N ligand on the emission wavelength is almost negligible when replacing *ppy* in [**1a**] and [**1b**] with *tolpy* in [**2a**] and [**2b**], respectively, or weak at the most when using *dfppy* ([**3a**] and [**3b**]) (Table 3).

The photoluminescent quantum yields (PLQYs) of complexes [**1a**]–[**3a**] are very high (75–95%) and better than that for their free ancillary pro-ligand **HL1** (63%). In contrast, the PLQYs of complexes [**1b**]–[**3b**] are comparatively lower (9–30%), though they largely exceed the PLQY of free **HL2** (0.2%). The luminescence lifetimes ($\tau_{1/2}$) of these phosphors in degassed acetonitrile at 25 ºC range between 308 and 748 ns. These long-lived excited states compare well with the respective values for other phosphorescent Ir(III) compounds,[10,57] which supports the triplet nature of the emission state and prognosticates an efficient photosensitization ability.[11] The photoluminescence spectra and $\tau_{1/2}$ of [**3a**] and [**3b**] were also recorded in deoxygenated H_2O/DMSO (96:4) at room temperature (Figure S8). Solvatochromic effects were not observed for these derivatives, though the luminescence lifetimes undergo important changes in aqueous media (see Table 3).

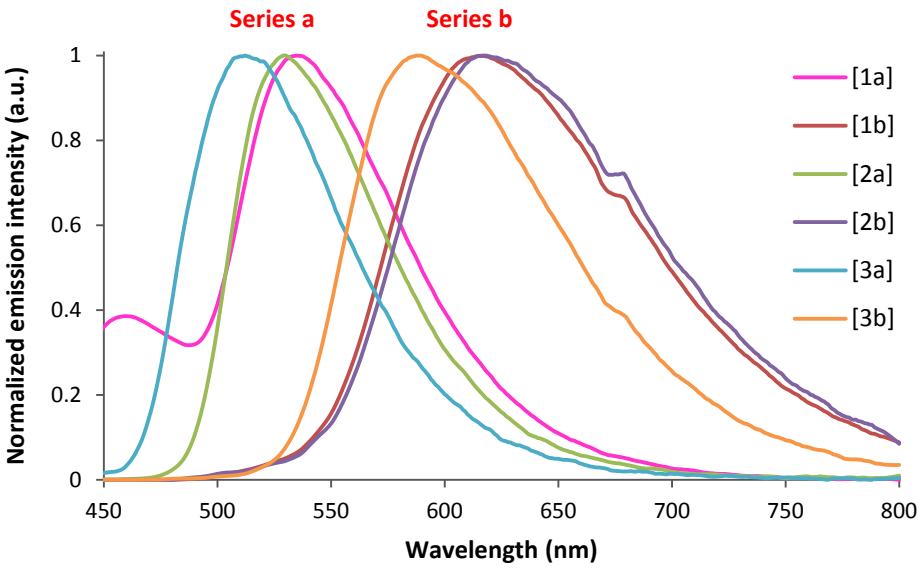

Figure 4. Overlaid emission spectra of complexes [**1a**]–[**3a**] and [**1b**]–[**3b**] in deoxygenated acetonitrile (10^{-5} M) at 25 °C. Excitation wavelengths (λ_{exc}) are given in Table 3.

Table 3. Photophysical data for complexes [**1a**]–[**3a**] and [**1b**]–[**3b**] in deoxygenated acetonitrile (10^{-4} M) at 25 °C.

Compound	λ_{exc} (nm)	λ_{em} (nm), 298 K	PLQY (%)	$\tau_{1/2}$ (ns)	λ_{em} (nm)[a]
HL1	338	457 (blue)	63	3.9	-
HL2	311	363 (UV)	0.2	< 1	-
[**1a**]	420	533 (2.33 eV), green	95	578	-
[**1b**][c]	469	605 (2.05 eV), orange	11	605	-
[**2a**]	399	527 (2.35 eV), green	75	384	-
[**2b**]	469	607 (2.04 eV), orange	9	748	-
[**3a**]	399	512 (2.42 eV), green	85	366 (115[b])	510
[**3b**]	451	580 (2.14 eV), orange	30	308 (975[b])	586, 613

[a] Recorded in deoxygenated H_2O/DMSO (96:4) (10^{-5} M) at 298 K. [b] The $\tau_{1/2}$ values in brackets were recorded in deoxygenated H_2O/DMSO (96:4) (10^{-5} M) at 298 K. [c] Photophysical properties of [**1b**] have been previously measured by Li and coworkers[39] in different conditions (λ_{em} = 602 nm; PLQY = 1.8% with reference to $[Ru(bpy)_3]^{2+}$; $\tau_{1/2}$ = 980 ns, for an air-equilibrated solution of [**1b**] (20 μM) in CH_2Cl_2 at r. t.).

Theoretical Calculations

To gain insight into the electrochemical and photophysical properties of these compounds, density functional theory (DFT) calculations were performed at the B3LYP/(6-31G*+LANL2DZ) level on the molecular and electronic structures of the $[Ir(C^N)_2(N^O)]$ complexes in the presence of the solvent (acetonitrile).

Figure 5 displays the contour plots and the energies computed for the frontier molecular orbitals (MOs) of **[1a]** and **[1b]**, as representative examples, at their electronic ground state (S_0) optimized geometries. The highest-occupied molecular orbital (HOMO) of both complexes is composed of a mixture of Ir(III) d_π orbitals (t_{2g}) and π orbitals of the phenoxy fragment of the (N^O) ligand. This is in contrast with the HOMO composition found for the well-known iridium(III) cationic complexes of general formula $[Ir(C^N)_2(N^N)]^+$ (C^N = *ppy*; N^N = diimine), for which the HOMO results from a mixture of Ir(III) d_π orbitals (t_{2g}) and π orbitals of the cyclometalating C^N ligands.[58–61] In contrast to the HOMO, significant differences are found between the LUMO of [**1a**] and [**1b**]. Whereas for complex [**1a**] the LUMO, and also the LUMO+1, resides on the C^N ligands, the LUMO of [**1b**] is mainly located on the N^O ligand and its topology corresponds to the LUMO of the free ligand. The topologies of the LUMO and LUMO+1 of [**1a**] actually correlate with those of the LUMO+1 and LUMO+2 of [**1b**], and the LUMO of [**1b**] is indeed analogous to the LUMO+2 of [**1a**] (Figure 5). Thus, the LUMO of the N^O ligand is strongly stabilized by 0.50 eV on going from [**1a**] to [**1b**]. This stabilization is likely due to the deficient electron donor ability of benzothiazole compared to benzimidazole, which in turn could be related to the weaker overlapping ability of the 3*p* orbital in the S atom of benzothiazole when compared with the 2*p* orbital of the N atom in benzimidazole.

The trends discussed above for the HOMO and LUMO of [**1a**] and [**1b**] are also observed for complexes [**2a**] and [**3a**] compared with [**2b**] and [**3b**] (Figure S9), and explain the experimental redox properties. On the one hand, the stabilization of the HOMO and LUMO by 0.09–0.12 and 0.20–0.27 eV, respectively, in passing from [**1a**]–[**3a**] to [**1b**]–[**3b**] justifies the higher oxidation potentials and the less negative reduction potentials measured for [**1b**]–[**3b**] (Table 1). On the other hand, the different nature of the LUMO suggests that reduction takes place first on the C^N ligands for complexes [**1a**]–[**3a**] and on the N^O ligand for [**1b**]–[**3b**]. This has been

10.1002/chem.201803784

ascertained by computing the anion species of [**1a**] and [**1b**], for which the extra electron is located on the C^N and N^O ligand, respectively. The higher stabilization undergone by the LUMO determines that the HOMO−LUMO energy gap decreases from 3.48−3.51 eV in [**1a**]–[**3a**] to 3.33−3.42 eV in [**1b**]–[**3b**] (Figure S9), in good agreement with the reduction of the electrochemical gap observed experimentally (Table 1). If the emitting triplet state T_1 is in a first approach assumed as originating from the HOMO → LUMO excitation, the calculated HOMO−LUMO gaps support the red-shift observed experimentally for the emission bands on going from [**1a**]–[**3a**] (λ_{em} = 512–533 nm) to [**1b**]–[**3b**] (λ_{em} = 580–605 nm).

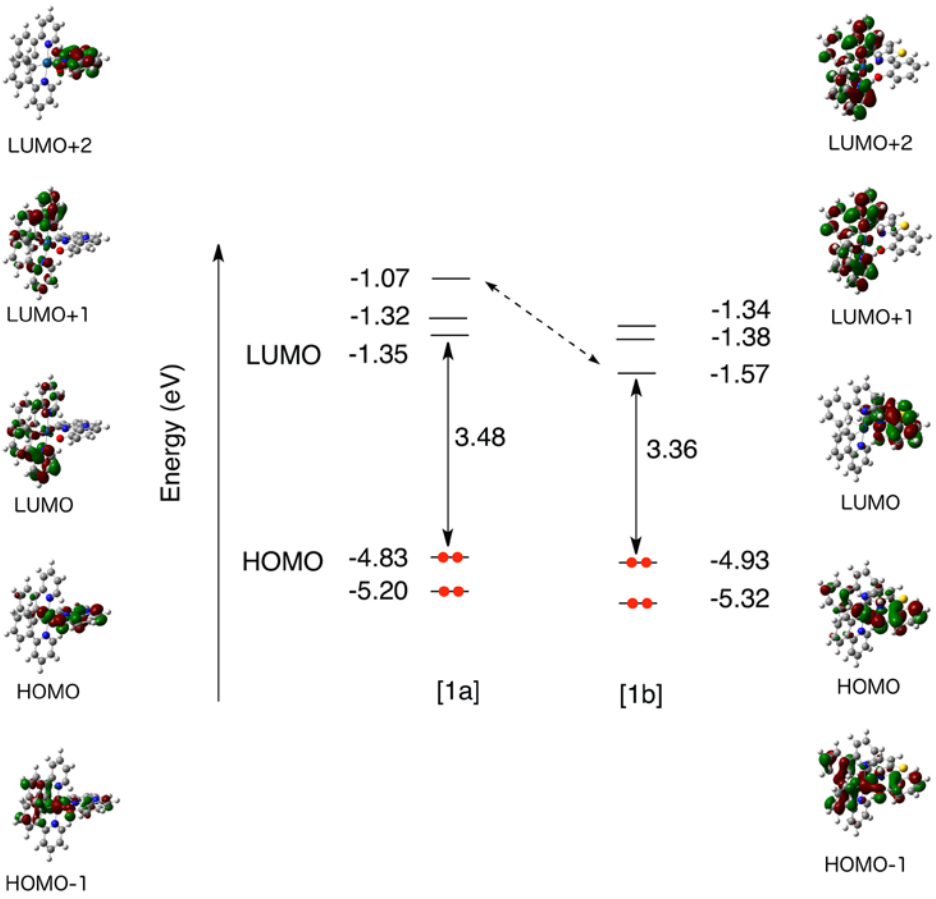

Figure 5. Schematic representation showing the energies and the isovalue contour plots calculated for the frontier molecular orbitals of **[1a]** and **[1b]**.

To investigate the nature of the electronic excited states participating in the absorption and emission processes, the low-lying excited states of all the complexes were calculated at the optimized geometries of the ground state (S_0) using the time-dependent DFT (TD-DFT) approach. Table S7 summarizes the vertical excitation energies calculated for the first three singlets and triplets, together with their molecular orbital description and electronic nature. The transitions to the singlet states above 400 nm present a low total oscillator strength (f = 0.02–0.03) for complexes [**1a**]–[**3a**], whereas the same transitions in complexes [**1b**]–[**3b**] show a significantly higher oscillator strength (f = 0.11–0.14). This explains the lower intensity observed in the UV-Vis spectra for complexes [**1a**]–[**3a**] above 400 nm (Figure 3). Concerning

10.1002/chem.201803784

the triplets, the three first triplet states of complexes [**1a**], [**2a**], and [**3a**] result from a combination of the HOMO → LUMO, LUMO+1, and LUMO+2 excitations and are predicted very close in energy in an interval of only 0.05, 0.06, and 0.15 eV, respectively. All the three states exhibit a ^{3}MLCT character, due to the participation of the Ir atom in the HOMO, mixed with ^{3}LLCT character, associated to the HOMO → LUMO and LUMO+1 excitations, and also ^{3}LC character due to the HOMO → LUMO+2 excitation involving the N^O ligand (see Figure 5). In contrast, for complexes [**1b**], [**2b**], and [**3b**] bearing the benzothiazole-based ligand **L2**, the low-lying triplet is well-separated by ~0.4 eV from the other triplet states and is mostly defined by the HOMO → LUMO excitation. Since this excitation mainly involves the N^O ligand (Figure 5), the T_1 state shows a predominant ^{3}LC nature with a small ^{3}MLCT character.

To get a deeper insight into the electronic nature of the emitting state, the lowest T_1 and T_2 triplet states of complexes [**1a**]–[**3a**] and the T_1 state of [**1b**]–[**3b**] were furthermore optimized at the spin-unrestricted UB3LYP level. Figure 6 displays the unpaired-electron spin-density distributions calculated for [**1a**] (T_1 and T_2) and [**1b**] (T_1) at their optimized geometries as representative examples. Complexes with the same ancillary ligand display analogous spin-density distributions (Figure S10). For complex [**1a**], T_1 features a ^{3}LC character with a spin-density distribution mainly centered on the ancillary N^O ligand (~1.86 unpaired electrons) and a small contribution from the Ir-*ppy* environment (~0.14e), thus matching the topology of the HOMO → LUMO+2 LC excitation. In contrast, T_2 shows a ^{3}LLCT/^{3}MLCT character, with a spin density spreading over the *ppy*-Ir environment (Ir 0.46e, C^N ligands 1.35e) and a little contribution of the N^O ligand (0.19e), mainly originating from the HOMO → LUMO LLCT/MLCT excitation. After full geometry relaxation, the T_1 and T_2 states are predicted to be almost isoenergetic (2.46 and 2.47 eV above S_0, respectively), and emission could indeed take place either from T_1 or T_2. Similar relative energies are also obtained for T_1 and T_2 in [**2a**] (2.45 and 2.48 eV) and [**3a**] (2.48 and 2.60 eV). For complexes [**1b**]–[**3b**], the T_1 triplet has no other triplet state close in energy and clearly shows a ^{3}LC nature (Figure 6) with a spin-density distribution mainly centered on the ancillary ligand (~1.78e) and a small contribution on the Ir-*ppy* environment (~0.22e). UB3LYP calculations therefore suggest that emission occurs from a triplet state with a predominant ^{3}LC nature for complexes [**1b**]–[**3b**], whereas it results from a combination of ^{3}MLCT/^{3}LLCT and ^{3}LC states for complexes [**1a**]–[**3a**]. The ^{3}LC nature (lower participation of the metal atom) and the lower energy (~2.10 eV) predicted for the emitting T_1 triplet of complexes [**1b**]–[**3b**] justifies the lower PLQYs recorded for these complexes (9–30%) compared with complexes [**1a**]–[**3a**] (75–95%) (Table 3).

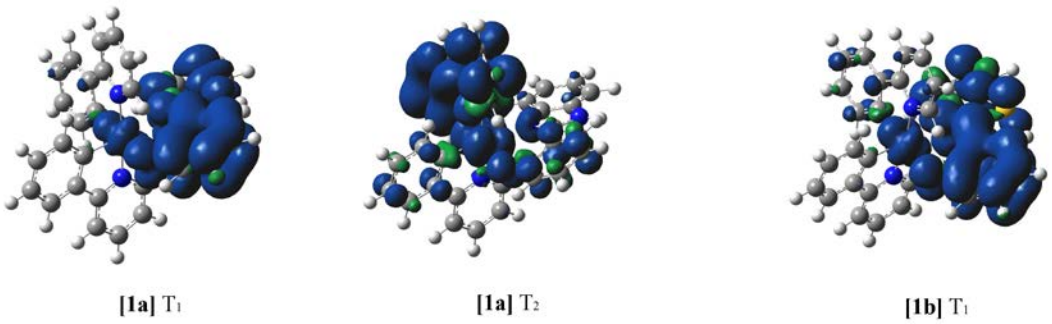

Figure 6. Spin-density contours calculated for fully relaxed T_1 and T_2 states of complex [**1a**] and T_1 state of complex [**1b**].

O_2-sensitive photo-luminescence

10.1002/chem.201803784

The O_2-sensitive photoluminescence of complexes [**1a**], [**2a**], and [**3a**] was visually proved by taking photographs of the corresponding deoxygenated solutions in acetonitrile (10^{-4} M) under UV light (365 nm) in the dark (Figure S11a), followed by slow diffusion of air (1 min) and then air-bubbling (1 min). Initially, the deoxygenated solutions exhibit strong photoluminescence, but then, after air exposure, an incipient quenching is observed in the high zone of the vials going down throughout the solution as a result of O_2 diffusion (Figure S11b), and finally a fast and dramatic switch off in the emission is witnessed after air-bubbling (Figure S11c). Then, the photoluminescence was switched on again by bubbling N_2 through the solutions for 1 minute (Figure S11d). This result establishes the reversibility of the process and suggests the potential use of these derivatives as PDT agents. Figure 7 shows the complete process of photoluminescence decay for **[2a]** as a result of O_2 diffusion during a period of 2 minutes. Consistently, the comparison of the photoluminescence emission spectra of complex **[2a]** in deoxygenated and oxygenated acetonitrile (10^{-4} M) at 25 ºC displays a dramatic drop in the intensity of the emission band for the latter (Figure S12). Furthermore, the O_2-sensitive nature of the emission process is consistent with a phosphorescent mechanism.[62]

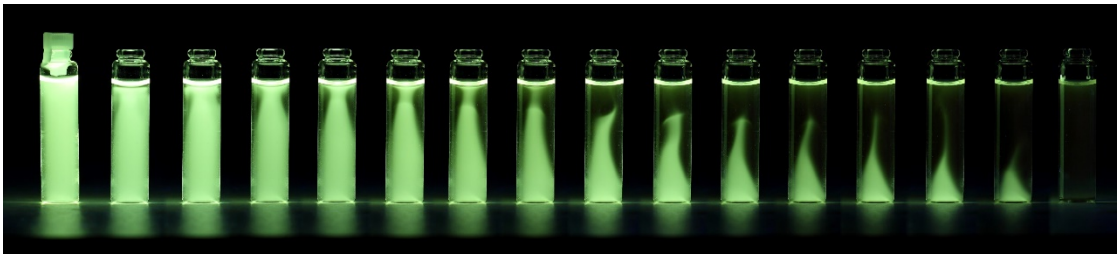

Figure 7. Sequence of photographs illustrating the quenching of photoluminescence under UV light (365 nm) for a solution of complex **[2a]** in acetonitrile (10^{-4} M) prepared under N_2 atmosphere in glove box as a result of O_2 diffusion during a period of 2 min.

Determination of quantum yields for the generation of $^1O_2$

Before performing the photocytotoxicity and catalytic photooxidation studies, we investigated the ability of the ligands and Ir complexes to produce $^1O_2$ and the quantum yields for its generation (ϕ_Δ) was calculated. Indeed, ϕ_Δ is the number of $^1O_2$ molecules formed per absorbed photon and to determine this parameter we studied the kinetics of the photooxidation of 1,3-diphenylisobenzofuran (DPBF) in terms of absorbance decrease at 410 nm as a function of irradiation time (λ_{iir} = 460 nm). The collected data – pairs yields a first order kinetic curve except for **HL1**, **HL2**, [**1b**] and [**2b**]. The kinetic constants (k) were obtained from the fitting of these kinetic traces to a single exponential equation (Figure S13). ϕ_Δ was calculated by comparison with a standard photosensitizer (methylene blue, MB), as follows: $\phi_{\Delta,comp} = \phi_{\Delta,MB} \cdot k_{comp}/k_{MB}$. Table 4 summarizes the obtained results. Interestingly, complexes [**1a**]–[**3a**] containing **L1** are the most efficient photosensitizers in the generation of $^1O_2$.

Table 4. Quantum yields for singlet oxygen generation (ϕ_Δ) for the different compounds used as photosensitizers in DMSO/H_2O (60:40)

Compound	ϕ_Δ
HL1	
HL2	
[**1a**]	1.05 ± 0.08
[**1b**]	
[**2a**]	1.12 ± 0.07

[**2b**]	
[**3a**]	0.86± 0.06
[**3b**]	0.78 ± 0.12
MB	0.52[a]

[a] Taken from ref: Chem. Commun., 2015,51, 10831-10834

Biological Studies

Cellular Uptake. The uptake of the ligands and their Ir(III) complexes in SW480 (colon adenocarcinoma) cells was investigated by bioimaging thanks to the emission properties of the complexes and by inductively coupled plasma mass spectrometry (ICP-MS). For the bioimaging approach, a microplate reader in phase contrast, blue, green and orange emission modes was used. None of the ligands were visualized inside the cells. By contrast, all of the Ir(III) complexes are successfully internalized in the cells (Figure 8).

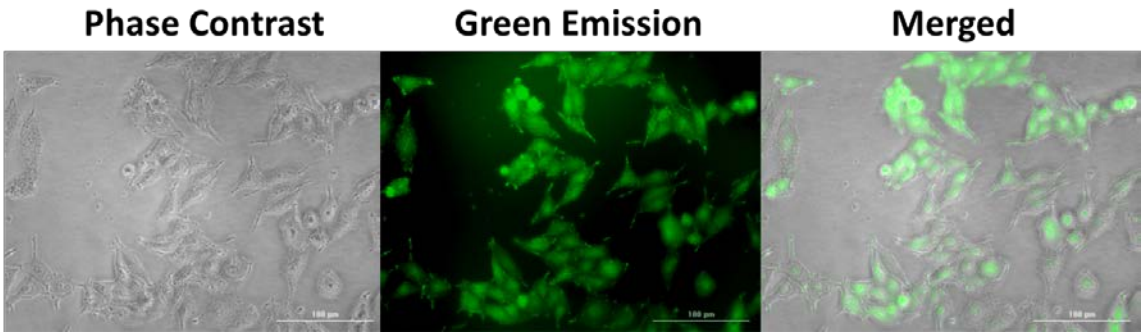

Figure 8. Example of the cellular uptake of Ir(III) complexes by SW480 cells. The images correspond to the uptake of complex **[1b]** at 50 µM within 10 minutes of incubation time.

In order to quantify the cellular internalization of the studied complexes, SW480 cells were treated with a 5 µM solution of each of these compounds during 24 h and ICP-MS measurements were performed. Iridium cellular accumulation is shown in Figure 9. There are no significant differences between series **a** and **b**, whereas there are substantial differences as a function of the C^N ligands that seem to be responsible for the complexes cellular uptake. Complexes bearing *dfppy* are the most internalized and those with *ppy* the less internalized.

According to recent reports in the literature, the cellular uptake of the PS depends not only on their net charge, but also on their charge distribution, lipophilicity and 3D structure.[63,64] Thus, it has been argued that positively charged PSs are attracted electrostatically to the vicinity of cell membranes by the negatively charged components of the phospholipid bilayer, so that it is only in the proximity of the membrane that hydrophobic interactions begin to operate favoring the uptake of compounds with low net charge. In particular all our complexes are neutral, which should be advantageous for their passive transport across membranes. However they exhibit different dipole moments according to theoretical calculations (see Table S8). Indeed, complexes with *dfppy* are more polar than their respective couples, which could facilitate the initial attraction to the proximity of cell membrane and might be related to their faster internalization in the SW480 cells.

Interestingly, all the new Ir derivatives are more accumulated inside the cells than the well-known anticancer agent cisplatin (CDDP).

10.1002/chem.201803784

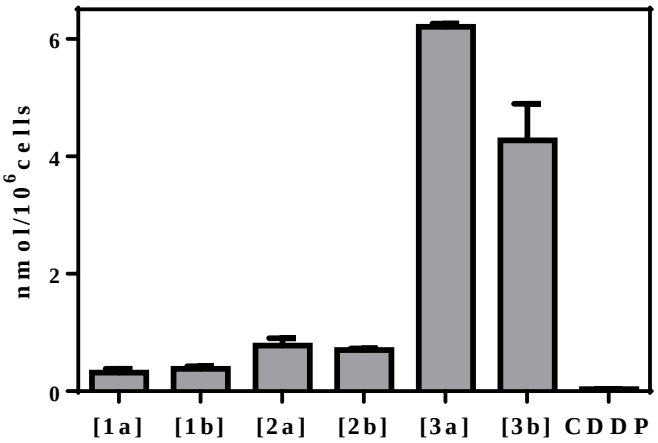

Figure 9. Iridium accumulation in SW480 cells treated with 5 μM solutions of the studied complexes during 24 h.

***Cytotoxicity and Photocytotoxicity*.** The cytotoxicity of both ligands and the Ir(III) complexes was studied in SW480 cells by means of the MTT proliferation assay with 24 h of exposure time in the dark and after 5 minutes of irradiation with either UV (λ= 365 nm, 8 mW cm^{-2}) or blue light (λ= 460 nm, 5.5 mW cm^{-2}). The IC_{50} values are summarized in Table 5.

Table 5. IC_{50} values in SW480 cells with 24 h of exposure time of the ligands and their Ir(III) complexes in the dark and after 5 min of irradiation with UV (λ= 365 nm, 8 mW cm^{-2}) or blue light (λ= 460 nm, 5.5 mW cm^{-2}).

Compound	IC_{50} Dark (μM)	IC_{50} UV light (μM)	IC_{50} Blue light (μM)
HL1	>100	>100	>100
HL2	>100	37.1 ± 4.7	>100
[**1a**]	>100	82.4 ± 14.4	42.9 ± 5.4
[**1b**]	7.4 ± 1.1	54.4 ± 10.2	7.7 ± 1.0
[**2a**]	>100	>100	50.0 ± 10.2
[**2b**]	7.0 ± 0.5	>100	7.6 ± 1.1
[**3a**]	>100	17.1 ± 0. 9	26.5 ± 0.9
[**3b**]	16.5 ± 5.7	46.5 ± 8.4	16.4 ± 0.70
CDDP	38.6 ± 1.4		

In the dark, neither the ligands nor the complexes of series **a**, bearing **L1** as the ancillary ligand, are cytotoxic. By contrast, the complexes of type **b**, with **L2** as the ancillary ligand, are more cytotoxic than CDDP, even though the cellular accumulation after 24 h is low for some of them, i.e., **[1b]** and **[2b]** (see Figure 9). Besides, the cytotoxic potency of **[2b]** in the dark is higher than that of **[3b]** despite the lower cellular accumulation of the former. Therefore, we can conclude that cellular accumulation has only a relative effect on the cytotoxicity of our Ir complexes in the dark. In addition, the images recorded in a bioimaging microplate reader (Fig. S14) show that the emission pattern of the complexes inside the cells depends on their ancillary ligand. Indeed, complexes of type **b** seem to be preferentially localized in the nucleus while complexes of type **a** do not manage to get into the nucleus remaining outside. Furthermore, complex **[3b]** exhibits a distribution pattern slightly different to that of **[1b]** and **[2b]**, since it is equally distributed throughout the cell. Consequently, the different subcellular localization of these derivatives as a function of the O^N ligand, mainly, and the C^N ligand, in second place,

could decisively determine their biomolecular targets and therefore, to their cytotoxic potency in the absence of light.

Now, if we observe the IC_{50} figures of series **b** under UV irradiation, we can verify that the cytotoxicity diminishes, such diminution being very sharp in the case of **[2b]**. As shown below, this behavior can be attributed to the release of the **HL2** ligand, whose cytotoxicity is less than that of the corresponding complexes. However, under blue light irradiation the IC_{50} values reported for this series remain unaltered regarding the values in the dark, meaning that the less energetic blue irradiation does not affect the stability of the complex.

Contrary to what has been observed with the complexes of series **b**, the complexes of series **a** are the most promising compounds for PDT purposes since all of them displayed negligible cytotoxicity in the dark that was significantly increased after UV and Vis irradiation. The most revealing result is that obtained for complex **[3a]** that not only enhanced its cytotoxic activity after irradiation with either UV or blue light, but also displayed higher activity than cisplatin (CDDP). Within the complexes of series **a**, **[3a]** is the most cytotoxic after irradiation, an outcome ascribable, in principle, to the greater internalization degree of this complex in the dark compared to **[1a]** and **[2a]** (Figure 9). Once inside the cell, the irradiation causes the cell death by a number of processes associated to PDT (but only for complexes of series **a**).

To properly learn some of the possible factors involved, the quantum yield in the $^1O_2$ generation (ϕ_Δ) can be considered. Table 4 shows that under Vis light, the efficiency in $^1O_2$ generation is quite high for series **a**. Hence, there is a good correlation between photo toxicity and ϕ_Δ for complexes of type **a** and, as a consequence, the observed phototoxicity could be related to the production of $^1O_2$ and other ROS. Nevertheless, the ϕ_Δ values obtained for one of the Ir(III) complexes bearing **L2** ([**3b**]) are not in good agreement with the photo-cytotoxicity results (as it does not exhibited increased cytotoxic activity when irradiated at 460 nm) even though it is rather efficient in the generation of singlet oxygen.

Stability studies

In order to clarify whether the new Ir(III) complexes are the actual species responsible for the observed cytotoxicity or photocytotoxicity we analysed their stability in the dark, under irradiation and at different pH values.

Stability in the dark. The stability of aqueous solutions of the ancillary pro-ligands (**HL1** and **HL2**) and all the Ir(III) complexes in the dark was experimentally corroborated by absorbance spectroscopy, since no changes were recorded in the respective spectra for a week.

Photostability. The photostability of ligands **HL1** and **HL2** and the respective Ir(III) complexes was studied by recording their absorbance spectra freshly prepared in aqueous solution and after 5 min of irradiation with UV (λ= 365 nm, 8 mW cm^{-2}) and blue light (λ= 460 nm, 5.5 mW cm^{-2}). Complexes of series **a** are stable after both irradiation periods since no changes in their UV-Vis spectra are observed, whereas the complexes of type **b** show variations in their spectra after UV light irradiation that suggest a certain degree of chemical evolution (Figures S15).

To identify the products resulting from photodegradation, the photo-stability of complexes [**3a**] and [**3b**] in solution ($3\cdot\times 10^{-4}$ M, DMSO-d_6) was studied by ^{1}H NMR over a period of 16 h under irradiation (blue light, LED, λ = 460 nm, 24 W) in an open-air tube. Both complexes showed a remarkable photo-stability during the first 8 h, since the ^{1}H NMR spectra of [**3a**] and [**3b**] remained essentially unchanged. However, incipient signals for the free ligand and the chloro-bridged Ir(III) dimer appeared after 12 h and are clearly visible after 16 h, giving

10.1002/chem.201803784

degradation values of 5 and 13% by integration for [**3a**] and [**3b**], respectively (Figures S16 and S17).

Stability of [1a] as a function of pH. The stability of the model complex [**1a**] as a function of pH was studied by ^{1}H NMR in the dark. Thus, the addition of an excess of NaOH over a solution of [**1a**] in DMSO-d_6 produces the extinction of the N−H resonance and the shifting of most of the signals in agreement with the formation of the anionic species, [**1a'**]$^-$ (See Scheme S1 and Figures S18-S19). On the other side, the acidification of a solution of [**1a**] in DMSO-d_6 with DCl gave rise to a mixture between the non-emissive complex [Ir(*ppy*)$_2$Cl(DMSO-d_6)] and the blue-emissive pro-ligand **HL1** (See Scheme S1 and Figures S20-S21). A similar acid-induced degradation has been reported for neutral complexes of general formula [Ir(C^N)$_2$(X^O)] (C^N = *ppy* or *dfppy*, X^O = picolinate or acetylacetonate).[41] Both processes, the acidic dissociation and the basic deprotonation, are reversible as it was shown by supplementary experiments. In addition, dramatic changes in the colour of the photo-luminescent emission (λ_{irr} = 365 nm) resulted from either acidification or alkalization of [**1a**], due to the formation of **HL1** (green to blue) or [**1a'**]$^-$ (green to orange), respectively.

Ir(III)-promoted Photooxidation of thioanisole and S-containing aminoacids

Aiming to get deeper into the mechanism of action of these derivatives, we studied their photocatalytic properties. Ir(III) tris- and bis-cyclometalated complexes are able to catalyze different photooxidation reactions[57,62,65,66] as a result of their ability to generate singlet oxygen ($^1O_2$) or superoxide ($O_2^{\bullet-}$).[20,67] In particular, Aoki et al. have shown that the photooxidation of thioanisole is promoted by Ir(III) tris-cyclometalated complexes of the type [Ir(C^N)$_3$] (C^N = phenylpyridinate ligands).[68] After confirming that our derivatives can generate $^1O_2$ as well (*vide supra*), we decided to test their ability to photocatalyze the above-mentioned reaction. Thus, we monitored by ^{1}H NMR the evolution of an oxygenated thioanisole solution (10 mM) in DMSO-d_6/D_2O (3:2) in the presence of complexes [**1a**]–[**3a**] and [**1b**]–[**3b**] (10^{-2} mM) illuminated with a blue LED strip (λ_{em} = 460 nm) at room temperature. In all the experiments the corresponding sulfoxide (methylphenylsulfoxide, MPS) was obtained selectively and the conversion depends strongly on both the ancillary and the cyclometalated ligands. Thus, photocatalysts [**3a**] and [**3b**] gave the highest conversion values (66 and 94% after 18 h, respectively) (Table 6).

Several control experiments were performed in order to delve into the nature of this reaction. In particular, the reaction was inhibited in the absence of Ir(III) PSs or light (see entries 9 and 10 in Table 6). Moreover, the reaction was also impeded when employing the free ligands or when using [**3a**] as potential PS but in the presence of NaN_3 ($^1O_2$ quencher)[28] (see entries 7, 8, and 11 in Table 6). All these results confirm the photocatalytic nature of this oxidation, the active role of the Ir(III) complexes as PSs and the key role of $^1O_2$ as the actual oxidant.

Table 6. Catalyst screening and control experiments in the photooxidation of thioanisole under an O_2 atmosphere and blue-LED irradiation

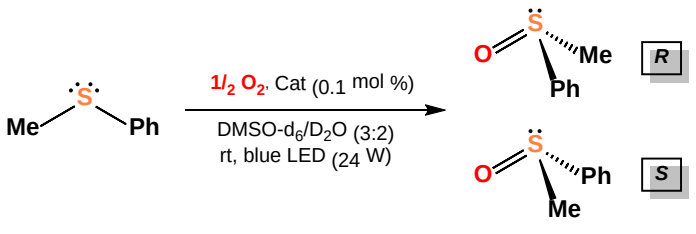

10.1002/chem.201803784

Entry	Conditions (Cat / Light / Gas)[a]	% Conv, 12 h (18 h)[b]
1	[**1a**] / Blue Light / O_2	31.1 (61.5)
2	[**1b**] / Blue Light / O_2	45.1 (61.3)
3	[**2a**] / Blue Light / O_2	31.1 (54.5)
4	[**2b**] / Blue Light / O_2	39.6 (47.2)
5	[**3a**] / Blue Light / O_2	49.5 (66.3)
6	[**3b**] / Blue Light / O_2	77.0 (94.0)
7	**HL1** / Blue Light / O_2	4.5
8	**HL2** / Blue Light / O_2	3.2
9	**No Cat** / Blue Light / O_2	0
10	[**3a**] / No Light / O_2	2.3
11	[**3a**] / Blue Light / O_2 / NaN_3[c]	0

[a] Thioanisole (10 mM), PS (10^{-2} mM, 0.1 mol %) in a mixture of DMSO-d_6/D_2O (0.5 mL, 3:2) at room temperature, under a saturated atmosphere of either O_2 or N_2 and under irradiation with blue light (LED, λ = 460 nm) in a septum-capped tube. [b] Conversion yields were determined by ^{1}H NMR analysis (see Figure ~~S21~~S22) of the crude mixture as average values of two independent experiments. [c] NaN_3 (11 mM).

In addition, complexes [**3a**] and [**3b**] were selected to assess their catalytic activity in the photooxidation of the sulfur-containing aminoacids, L-methionine and L-cysteine. The conversion values (%), collected in Table 7, demonstrate that [**3a**] and [**3b**] are efficient promoters in the chemoselective oxidation of both aminoacids to methionine sulfoxide and cystine respectively. Control experiments in the absence of PS confirmed the photocatalytic role of the Ir(III) derivatives in these transformations, though in the case of the easily oxidized L-cysteine, partial oxidation also takes place in the absence of PS. These results suggest a possible mechanism of action based on the photooxidation of proteins at least for [**3a**].

Table 7. Photooxidation of L-methionine or L-cysteine under an O_2 atmosphere and blue-LED irradiation

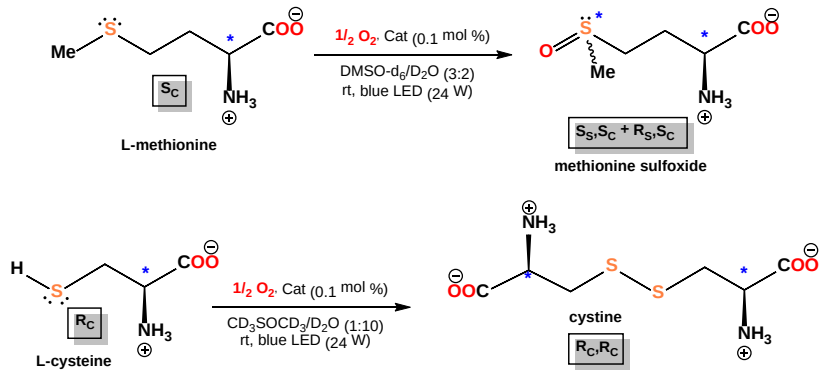

Entry	Substrate	Conditions[a]	% Conv, 12 h (18 h)[b]
1	L-Met	[**3a**] / Blue light / O_2	48 (71)
2	L-Met	[**3b**] / Blue light / O_2	100
3	L-Met	No Cat / Blue light / O_2	0
4	L-Cys	[**3a**] / Blue light / O_2	90
5	L-Cys	[**3b**] / Blue light / O_2	82
6	L-Cys	No Cat / Blue light / O_2	44

[a] L-methionine/L-cysteine (10 mM), PS (10^{-2} mM, 0.1 mol %) in a mixture of DMSO-d_6/D_2O (0.5 mL, 3:2 or 1:10 respectively) at room temperature, under a saturated atmosphere of O_2 and under irradiation with blue light (LED, λ = 460 nm) in a septum-capped tube. [b] Conversion yields were determined by ^{1}H NMR analysis (see Figure ~~S22~~S23) of the crude mixture as average values of two independent experiments.

Conclusions

In the present paper, we disclose the synthesis and characterization of six neutral Ir(III) bis-cyclometalated complexes with two N^O ligands (2-(benzimidazolyl)phenolate (**L1**) and 2-(benzothiazolyl)phenolate (**L2**)) and three different cyclometalated ligands. We show that the photophysical and electrochemical properties of the described complexes depend preeminently on the N^O ligand with a minor influence corresponding to the cyclometalated ligand. For instance, the photoluminescent quantum yields are very high for those complexes with **L1** and moderately high or low for those complexes with **L2**. Besides, the emission wavelengths of the Ir(III) complexes are also strongly dependent on the specific N^O ligand, so that **L1** causes a marked blue-shift (between 68 and 80 nm) compared to **L2** in the emission of their respective complexes. These effects are thoroughly explained from theoretical calculations.

The *in vitro* cytotoxicity studies carried out with the described Ir(III) complexes on SW480 (colon adenocarcinoma) cells demonstrate that derivatives of type **a** (with **L1**) and **b** (with **L2**) exhibit very different biological activities. In particular, complexes of type **a** are innocuous against SW480 cells in the dark but display enhanced cytotoxicity after irradiation with UV or blue light. Specifically, complex [**3a**] with 2-(4,6-difluorophenyl)pyridinate as the C^N ligand has been recognized as the most efficient photosensitizer for PDT, likely due to a combination of several properties, such as high cellular uptake, good photostability, high quantum yield, long triplet excited state lifetime, high ability for $^1O_2$ production, and significant catalytic activity in the oxidation of S-containing L-amino-acids. On the contrary, complexes of type **b** are very cytotoxic in the dark likely owing to their subcellular localization, though they are inefficient PS agents for PDT due to their inefficiency in $^1O_2$ production and poor photostability upon UV irradiation. Moreover, the results obtained in this work suggest that within these two series of complexes the ancillary ligand is the main factor affecting the cytotoxic activity whereas the C^N ligands seem to control their cellular uptake.

To conclude, these compounds offer versatile properties as potential anticancer drugs and deserve deeper studies in order to better understand the strong effects on the anticancer properties derived from the subtle structural change in the O^N ligand.

Acknowledgements

We gratefully acknowledge the financial support provided by the Spanish Ministerio de Economía y Competitividad - FEDER (CTQ2014-58812-C2-1-R and CTQ2014-58812-C2-2-R, CTQ2015-70371-REDT, CTQ2015-71353-R, CTQ2015-71154-P, and Unidad de Excelencia María de Maeztu MDM-2015-0538), the Consejería de Educación – Junta de Castilla y León - FEDER (BU299A12-1, BU042U16 and BU051U16). The Generalitat Valenciana (Prometeo2016/135), and the Obra Social "la Caixa" (OSLC-2012-007).

EXPERIMENTAL PART

General Methods and starting materials.

Starting materials. $IrCl_3 \cdot xH_2O$ was purchased from Johnson Mattey and used as received. The starting dimers $[Ir(\mu\text{-}Cl)(C\text{^}N)_2]_2$ (C^N = *2*-phenylpyridinate, *ppy*; 2-(p-tolyl)pyridinate, *tolpy*; 2-(2,4-difluorophenyl)pyridinate, *dfppy*) were prepared according to the reported procedure.[38] The pro-ligands 2-phenylpyridine, 2-(p-tolyl)pyridine, 2-(2,4-difluorophenyl)pyridine, 2-(2-

hydroxyphenyl)-1*H*-benzimidazole (**HL1**) and 2-(2-hydroxyphenyl)benzothiazole (**HL2**) were purchased from Sigma-Aldrich and used without further purification. Deuterated solvents (CD_3SOCD_3, THF-d_8, $CDCl_3$, D_2O) were obtained from Euriso-top. Conventional solvents such as acetonitrile (Fisher Scientific or HPLC, Prolabo), diethyl ether (Fisher Scientific), acetone (Fisher Scientific) and 2-ethoxyethanol (Acros Organics) were degassed and in some cases distilled prior to be used. Tetrabutylammonium hexafluorophosphate ($[^nBu_4N][PF_6]$) was purchased from Acros.

Synthesis methods and characterization of complexes. All synthetic manipulations were carried out under an atmosphere of dry, oxygen-free nitrogen using standard Schlenk techniques. The solvents were dried and distilled under nitrogen atmosphere before use. Elemental analyses were performed with a Thermo Fisher Scientific EA Flash 2000 Elemental Microanalyzer. The analytical data for the new compounds were obtained from crystalline samples when possible. In some cases, the data were reasonably accurate, but in others the agreement of calculated and found values for carbon was > 0.4%, so that solvent molecules were introduced in the molecular formulae to improve agreement. IR spectra were recorded on a Jasco FT/IR-4200 spectrophotometer (4000–400 cm^{-1} range) with Single Reflection ATR Measuring Attachment. FAB(+) Mass spectra (position of the peaks in Da) were recorded with an Autospec spectrometer. The experimentally obtained m/z values are expressed in Da and the isotopic distribution matches that of calculated fragments. NMR samples were prepared under a nitrogen atmosphere by dissolving the suitable amount of compound in 0.5 mL of the respective oxygen-free deuterated solvent and the spectra were recorded at 298 K on a Varian Unity Inova-400 (399.94 MHz for ^1H; 376.29 MHz for ^{19}F; 100.6 MHz for ^{13}C). Typically, ^1H NMR spectra were acquired with 32 scans into 32 k data points over a spectral width of 16 ppm. ^1H and $^{13}C\{^1H\}$ chemical shifts were internally referenced to TMS via the residual ^1H and ^{13}C signals of CHD_2SOCD_3 (δ = 2.50 ppm and δ = 39.52 ppm), $CHCl_3$ (δ = 7.26 ppm and δ = 77.16 ppm), THF-d_7 (δ = 1.72, 3.58 ppm and δ = 67.21, 25.31 ppm) for CD_3SOCD_3, $CDCl_3$ and THF-d_8, respectively, according to the values reported by Fulmer et al.[69] Chemical shift values (δ) are reported in ppm and coupling constants (*J*) in Hertz. The splitting of proton resonances in the reported ^1H NMR data is defined as s = singlet, d = doublet, t = triplet, st = pseudotriplet, q = quartet, sept = septet, m = multiplet, bs = broad singlet. 2D NMR spectra such as ^1H-^1H gCOSY, ^1H-^1H NOESY, ^1H-^{13}C gHSQC and ^1H-^{13}C gHMBC were recorded using standard pulse sequences. The probe temperature (±1 K) was controlled by a standard unit calibrated with methanol as a reference. All NMR data processing was carried out using MestReNova version 10.0.2.

X-ray Crystallography. A summary of crystal data collection and refinement parameters for [**3a**] are given in Table S2. A single crystal of [**3a**] was coated in high-vacuum grease, mounted on a glass fiber, and transferred to a Bruker SMART APEX CCD-based diffractometer equipped with a graphite monochromated Mo-Kα radiation source (λ = 0.71073 Å). The highly redundant datasets were integrated using SAINT[70] and corrected for Lorentz and polarization effects. The absorption correction was based on the function fitting to the empirical transmission surface as sampled by multiple equivalent measurements with the program SADABS.[71]

The software package WINGX[72] was used for space group determination, structure solution, and refinement by full-matrix least-squares methods based on F^2. A successful solution by direct methods provided most non-hydrogen atoms from the E-map. The remaining non-hydrogen atoms were located in an alternating series of least-squares cycles and difference Fourier maps. All non-hydrogen atoms were refined with anisotropic displacement coefficients. Hydrogen atoms were placed using a “riding model” and included in the refinement at calculated positions. CCDC reference number for **[3a]** is 1857871.

Measurements of UV-vis Absorption and Luminescence Spectra

UV-vis absorption spectra were recorded on a UVIKON XS UV-vis spectrophotometer, while excitation and emission spectra were recorded on a PTI Quanta Master TM spectrofluorometer from Photon Technology International equipped with a 75 W xenon short arc lamp and a model 814PTM detection system. Felix32 software was used to collect and process fluorescence data. Samples of 10^{-4} M solutions in CH_3CN were prepared in a globe-box under nitrogen atmosphere and the solutions were kept under inert atmosphere in quartz cuvettes equipped with Teflon septum screw caps for all the luminescence measurements. The emission and excitation slit widths were either 1 or 3 nm, depending on the emission intensity of the compounds, to avoid saturation of the detector. All optical measurements were made at room temperature or 77 K.

The luminescence emission spectra were first recorded by exciting at the maximum absorption wavelength of the corresponding UV-Vis absorption spectra. Once the maximum emission wavelength is determined in this experiment, an excitation scan for this emission was carried out to determine the maximum excitation wavelength, which was used later on to obtain the optimized emission spectra.

The emission quantum yield (PLQY or Φ) was calculated for each complex according to the equation:[73]

$$\Phi_s = \Phi_r \times (I_s/I_r) \times (A_r/A_s)$$

where Φ_s is the quantum yield of the sample, A_s and A_r are the absorbance of the sample and the reference at the excitation wavelength, and I_s and I_r represent the points of maximum intensity in the corrected emission spectra. Φ_r is the quantum yield for the reference complex, $[Ir(ppy)_2(bpy)](PF_6)$, which is assumed to be 7.07 in the experimental conditions.[74]

For the determination of the luminescence lifetime of compound [**1a**], the fluorescence decay was measured on a Photon Technology International (PTI) Time Master fluorimeter equipped with a picosecond nitrogen laser and a wavelength selector that was used with the dye 2-(4-biphenylyl)-6-phenylbezoxazole (PBBO). Astroboscopic detector was coupled to a Czerny-Turner monochromator on the emission port. The system was connected to a PC via an Ethernet interface and governed via Felix32. The instrumental parameters used were as follows: λ_{ex} = 396 nm, λ_{em} = 534 nm, 300 channels, integration time = 50 μs, 15 averages per decay, 5 shots per channel, laser pulse frequency = 5 Hz, 1 nm excitation and emission slit widths, and a logarithmic collection step.

Electrochemical measurements. Electrochemical measurements were performed using a customized SPELEC (DropSens) equipment, a commercial fully integrated synchronized spectroelectrochemical device that includes a bipotentiostat/galvanostat controlled by DropView (DropSens). All experiments were carried out using a three-electrode cell using a glassy carbon-disc with a diameter of 3 mm as working electrode, a platinum-wire as auxiliary electrode, and a silver-wire pseudo-reference electrode. Oxygen was removed from the solution by bubbling argon for 10 minutes and keeping the current of argon along the whole experiment. The formal potentials were determined by cyclic voltammetry (CV), scanning the potential at a scan rate of 0.1 V s^{-1}. All potentials were referred to the redox pair ferrocene/ferrocenium (Fc/Fc^+) took as internal standard. All voltammetric experiments were started and finished at a potential of −0.55 V and performed in a clockwise direction. Acetonitrile solutions of the complexes ($3\cdot\times 10^{-4}$ M) were used in the presence of $[^nBu_4N][PF_6]$ (0.1 M) as supporting electrolyte.

Theoretical Calculations. Density functional theory (DFT) calculations were carried out with the D.01 revision of the Gaussian 09 package,[75] using the Becke's three-parameter B3LYP

exchange-correlation functional,[76,77] together with the 6-31G(d) basis set for H, C, N, O, F, and S,[78,79] and the "double-ζ" quality LANL2DZ basis set for the Ir element.[80] The geometries of the singlet ground state (S_0) and the lowest-energy triplet state (T_1) were fully optimized without imposing any symmetry restriction. The geometries of the triplet states were calculated at the spin-unrestricted UB3LYP level with a spin multiplicity of 3. All the calculations were performed in the presence of the solvent (acetonitrile). Solvent effects were considered within the self-consistent reaction field (SCRF) theory using the SMD keyword that performs a polarized continuum model (PCM)[81] calculation using the solvatation model of Thrular et al.[82] Time-dependent DFT (TD-DFT) calculations of the lowest-lying 15 singlets and triplets were performed in the presence of the solvent at the minimum-energy geometry optimized for the ground state (S_0).

Determination of singlet oxygen generation The $^1O_2$ generation was verified by monitoring the photooxidation of 1,3-diphenylisobenzofuran (DPBF, 97 %, Sigma Aldrich, USA) by absorbance measurements as a function of the irradiation time. The irreversible interaction of DPBF with $^1O_2$ leads to a decrease in the absorbance of the DPBF band centered at 410 nm as a consequence of the 1,4-cycloaddition.[83] Stock solution of all the compounds, methylene blue (MB) used as standard and DPBF were freshly prepared in DMSO. The final concentration of all the compounds including the standard in the cuvette was 10 μM, and that of DPBF 50 μM in DMSO:H_2O (60:40). The absorbance was first recorded in a double beam Evolution 300 UV-Vis spectrophotometer (Thermo Scientific) and then after different times of irradiation with continuous aeration. The irradiation was performed by means of a Xenon short arc lamp (Ushio) with an intensity of 150 W, coupled with a monocromator fixed at 460 nm and slits at 5 nm. The decrease of the absorbance caused by photobleaching of DPBF was measured and corrected in all experiments.

Cellular Imaging

Approximately 1×10^4 SW480 colon adenocarcinoma cells were cultured in 200 μL Dulbecco's Modified Eagle's Medium per well supplemented with 10% fetal bovine serum and 1% amphotericin-penicillin-streptomycin solution (all from Sigma Aldrich) in 96-well plates and incubated at 37 °C under a 5% CO_2 atmosphere. The cells were grown for 24h and then exposed to 50 μM of the studied compounds. Then, the cells were visualized in a Cytation 5 Cell Imaging Multi-Mode Reader (Biotek Instruments, USA) in phase contrast, blue, green and orange fluorescence emission with a 20× objective.

Photocytotoxicity

Approximately 1×10^4 SW480 colon adenocarcinoma cells were cultured in 200 μL Dulbecco's Modified Eagle's Medium per well supplemented with 10% fetal bovine serum and 1% amphotericin-penicillin-streptomycin solution (all from Sigma Aldrich) in 96-well plates and incubated at 37 °C under a 5% CO_2 atmosphere. After 24h of incubation, the cells were exposed to different concentrations of the studied compounds and incubated for other 60 minutes. Then, the cells were irradiated during 5 minutes with UV light (at 365 nm, 8 mW cm^{-2}) or with blue light (at 460 nm, 5.5 mW cm^{-2}) and incubated again for other 24h. After that, cells were incubated with 100 μL of MTT (3-(4,5-dimethyltiazol-2-yl)-2,5-diphenyltetrazoliumbromide) (Sigma Aldrich) dissolved in culture medium (500 μg mL^{-1}) for a further period of 3 hours. At the end of the incubation, the formazan was dissolved by adding 100 μL of solubilizing solution (10% SDS, 0.01 M HCl) to each well. Absorbance was read after 18h of incubation at 590 nm in a microplate reader (Cytation 5 Cell Imaging Multi-Mode Reader (Biotek Instruments, USA). Four replicates per dose were included. The IC_{50} values were calculated from cell survival data using nonlinear regression of the GraphPadPrism Software Inc. (version 6.01) (USA). The IC_{50} values are the mean of at least two independent experiments.

Cellular uptake

SW480 cells were seeded in 12-well plates (1.5×10^5 cells/well) and grown for 24h. Then, cells were exposed to 5 μM of the studied metal complexes during 24h. Before analysis cells were washed three times with DPBS (Dulbecco's Phosphate Buffered Saline), then they were trypsinized and centrifugated. The pellets were resuspended in 1 mL of DPBS. In each case, 10 μL were used to count cells. Then, cells were digested for ICP-MS with 65% HNO_3 during 24h. Finally, solutions were analyzed in a 7700 ICP-MS (Agilent Technologies). Data are reported as the mean ± the standard deviation (n = 3).

Stability in the dark

Aqueous solutions (15 μM) of every compound were prepared and monitored by UV-vis spectroscopy during a week while kept at room temperature and protected from light. No changes in the UV-vis spectra were observed.

Photostability

15 μM fresh aqueous solutions of the studied complexes were prepared. Their absorbance were monitored in a Hewlett-Packard 8453A (Agilent Technologies, Palo Alto, CA) photodiode array spectrophotometer fitted out with a Peltier temperature control system, at 25.0 °C. Then, the solutions were irradiated during 5 minutes with UV light (at 365 nm, 8 mW cm^{-2}) or with blue light (at 460 nm, 5.5 mW cm^{-2}). Absorbance spectra were collected after each irradiation period.

Stability of [1a] as a function of pH

Alkalization: An aqueous solution of NaOH (0.5 M, 1.4 μL) was added to a solution of [**1a**] (4 mM, 0.5 mL) in DMSO-d_6 and the evolution of the mixture was monitored by NMR during 30 minutes. Then, an excess of NaOH (0.5 M, additional 1.6 μL) was added to the mixture. Finally, DCl (1 M in D_2O, 3 μL) was added over the same NMR tube to check the reversibility of the process (Figures S18 and S19).

Acidification: A solution of DCl (1 M in D_2O, 3 μL) was added to a solution of [**1a**] (4 mM, 0.5 mL) in DMSO-d_6 and the evolution of the mixture was monitored by NMR. Finally, NaOH (0.5 M aq. sol. in D_2O, 20 μL) was added over the same NMR tube to check the reversibility of the process (Figures S20 and S21).

General procedure for the catalytic photooxidation of thioanisole and L-aminoacids

Aliquots of stock solutions of the S-containing substrate in D_2O and the Ir(III) PS in DMSO-d_6 were added to a 5 mL test tube to achieve final concentrations of 10 mM (1 equiv) and 10^{-2} mM, (0.1 mol %, 10^{-3} equiv) respectively in a mixture DMSO-d_6/D_2O (0.5 mL, 3:2 or 1:10 for cysteine). The test tube is capped with a septum and the mixture is saturated with an atmosphere of O_2 using a needle and a balloon and then stirred at room temperature under irradiation with blue light at a distance of 4 cm from a flexible blue LED strip (AIGOSTAR MODEL SL02-RGB, λ = 460 nm, 24 W, 600 lm, 150 LEDs, 5 m). Conversion yields were determined by ^{1}H NMR analysis (see Figures S22 and S23) of the crude mixture as average values of two independent experiments. ESI MS spectra were recorded to confirm the identity of all the products. Methyl phenyl sulfoxide was obtained as a racemic mixture (enantiomers S_S and R_S), cystine was obtained as the (R,R) diastereomer, and methionine sulfoxide was obtained as a 1:1 mixture of diastereoisomers which are epimers at the sulfur atom, that is (S_S,S_C) and (R_S,S_C). Overoxidation to the corresponding sulfone products (thioanisole or methionine) or cysteine sulfenic, sulfinic or sulfonic acids were not detected in any experiment. NaN_3 was added in the respective control experiments to achieve a final concentration of 11 mM. A turbid suspension was obtained after stopping the reaction for cystine.

Bibliography

[1] P. Agostinis, K. Berg, K. A. Cengel, T. H. Foster, A. W. Girotti, S. O. Gollnick, S. M. Hahn, M. R. Hamblin, A. Juzeniene, D. Kessel, M. Korbelik, J. Moan, P. Mroz, D. Nowis, J. Piette, B. C. Wilson, J. Golab, *CA Cancer J. Clin.* **2011**, *61*, 250–281.

[2] J. D. Knoll, C. Turro, *Coord. Chem. Rev.* **2015**, *282–283*, 110–126.

[3] N. Wu, J.-J. Cao, X.-W. Wu, C.-P. Tan, L.-N. Ji, Z.-W. Mao, *Dalton Trans.* **2017**, *46*, 13482–13491.

[4] D. E. Dolmans, D. Fukumura, R. K. Jain, *Nat. Rev. Cancer* **2003**, *3*, 380–387.

[5] L. N. Lameijer, D. Ernst, S. L. Hopkins, M. S. Meijer, S. H. C. Askes, S. E. Le Dévédec, S. Bonnet, *Angew. Chem. Int. Ed.* **2017**, *56*, 11549–11553.

[6] A. Presa, R. F. Brissos, A. B. Caballero, I. Borilovic, L. Korrodi-Gregório, R. Pérez-Tomás, O. Roubeau, P. Gamez, *Angew. Chemie Int. Ed.* **2015**, *54*, 4561–4565.

[7] J. M. Dąbrowski, B. Pucelik, A. Regiel-Futyra, M. Brindell, O. Mazuryk, A. Kyzioł, G. Stochel, W. Macyk, L. G. Arnaut, *Coord. Chem. Rev.* **2016**, *325*, 67–101.

[8] P. R. Ogilby, *Chem. Soc. Rev.* **2010**, *39*, 3181–3209.

[9] X. Jiang, N. Zhu, D. Zhao, Y. Ma, *Sci. China Chem.* **2016**, *59*, 40–52.

[10] J. S. Nam, M.-G. Kang, J. Kang, S.-Y. Park, S. J. C. Lee, H.-T. Kim, J. K. Seo, O.-H. Kwon, M. H. Lim, H.-W. Rhee, et al., *J. Am. Chem. Soc.* **2016**, *138*, 10968–10977.

[11] A. Frei, R. Rubbiani, S. Tubafard, O. Blacque, P. Anstaett, A. Felgenträger, T. Maisch, L. Spiccia, G. Gasser, *J. Med. Chem.* **2014**, *57*, 7280–7292.

[12] P. I. Djurovich, D. Murphy, M. E. Thompson, B. Hernandez, R. Gao, P. L. Hunt, M. Selke, *Dalt. Trans.* **2007**, *34*, 3763–3770.

[13] M. Rajendran, *Photodiagn. Photodyn.* **2016**, *13*, 175–187.

[14] Y. Zheng, A. S. Batsanov, M. a. Fox, H. a. Al-Attar, K. Abdullah, V. Jankus, M. R. Bryce, A. P. Monkman, *Angew. Chemie* **2014**, *126*, 11800–11803.

[15] C. D. Ertl, C. Momblona, A. Pertegás, J. M. Junquera-Hernández, M.-G. La-Placa, A. Prescimone, E. Ortí, C. E. Housecroft, E. C. Constable, H. J. Bolink, *J. Am. Chem. Soc.* **2017**, *139*, 3237–3248.

[16] M. Martínez-Alonso, J. Cerda, C. Momblona, A. Pertegás, J. M. Junquera-Hernández, A. Heras, A. M. Rodríguez, G. Espino, H. Bolink, E. Ortí, *Inorg. Chem.* **2017**, *56*, 10298–10310.

[17] P. Steunenberg, A. Ruggi, N. S. Van Den Berg, T. Buckle, J. Kuil, F. W. B. Van Leeuwen, A. H. Velders, *Inorg. Chem.* **2012**, *51*, 2105–2114.

[18] J. H. Kang, H. J. Kim, T.-H. Kwon, J.-I. Hong, *J. Org. Chem.* **2014**, *79*, 6000–6005.

[19] T. Yoshihara, S. Murayama, T. Masuda, T. Kikuchi, K. Yoshida, M. Hosaka, S. Tobita, *J. Photochem. Photobiol. A Chem.* **2015**, *299*, 172–182.

[20] X. Jiang, J. Peng, J. Wang, X. Guo, D. Zhao, Y. Ma, *ACS Appl. Mater. Interfaces* **2016**, *8*, 3591–3600.

[21] L. He, Y. Li, C.-P. Tan, R.-R. Ye, M.-H. Chen, J.-J. Cao, L.-N. Ji, Z.-W. Mao, *Chem. Sci.* **2015**, *6*, 5409–5418.

[22] M. Ouyang, L. Zeng, K. Qiu, Y. Chen, L. Ji, H. Chao, *Eur. J. Inorg. Chem.* **2017**, *2017*, 1764–1771.

[23] W. Lv, Z. Zhang, K. Y. Zhang, H. Yang, S. Liu, A. Xu, S. Guo, Q. Zhao, W. Huang, *Angew. Chem. Int. Ed.* **2016**, *55*, 9947–9951.

[24] J. Liu, C. Jin, B. Yuan, X. Liu, Y. Chen, L. Ji, H. Chao, *Chem. Commun. (Cambridge, United Kingdom)* **2017**, *53*, 2052–2055.

[25] S. Mandal, D. K. Poria, R. Ghosh, P. S. Ray, P. Gupta, *Dalt. Trans.* **2014**, *43*, 17463–17474.

[26] L. K. McKenzie, I. V. Sazanovich, E. Baggaley, M. Bonneau, V. Guerchais, J. A. G. Williams, J. A. Weinstein, H. E. Bryant, *Chem. - Eur. J.* **2017**, *23*, 234–238.

[27] Y. Li, C.-P. C.-P. Tan, W. Zhang, L. He, L.-N. L.-N. Ji, Z.-W. Z.-W. Mao, *Biomaterials* **2015**, *39*, 95–104.

[28] A. Nakagawa, Y. Hisamatsu, S. Moromizato, M. Kohno, S. Aoki, *Inorg. Chem.* **2014**, *53*, 409–422.

[29] A. Kando, Y. Hisamatsu, H. Ohwada, T. Itoh, S. Moromizato, M. Kohno, S. Aoki, *Inorg. Chem.* **2015**, *54*, 5342–5357.

[30] S. Moromizato, Y. Hisamatsu, T. Suzuki, Y. Matsuo, R. Abe, S. Aoki, *Inorg. Chem.* **2012**, *51*, 12697–12706.

[31] V. Novohradsky, A. Zamora, A. Gandioso, V. Brabec, J. Ruiz, V. Marchán, *Chem. Commun.* **2017**, *53*, 5523–5526.

[32] A. Zamora, G. Vigueras, V. Rodríguez, M. D. Santana, J. Ruiz, *Coord. Chem. Rev.* **2018**, *360*, 34–76.

[33] J. Yellol, S. A. Pérez, G. Yellol, J. Zajac, A. Donaire, G. Vigueras, V. Novohradsky, C. Janiak, V. Brabec, J. Ruiz, *Chem. Commun.* **2016**, *52*, 14165–14168.

[34] C. Pérez-Arnaiz, M. I. Acuña, N. Busto, I. Echevarría, M. Martínez-Alonso, G. Espino, B. García, F. Domínguez, *Eur. J. Med. Chem.* **2018**, *157*, 279–293.

[35] J. Sun, J. Zhao, H. Guo, W. Wu, *Chem. Commun.* **2012**, *48*, 4169–4171.

[36] Y. You, J. Seo, S. H. Kim, K. S. Kim, T. K. Ahn, D. Kim, S. Y. Park, *Inorg. Chem.* **2008**, *47*, 1476–1487.

[37] M. Nonoyama, *Bull. Chem. Soc. Jpn.* **1974**, *47*, 767–768.

[38] S. Sprouse, K. A. King, P. J. Spellane, R. J. Watts, *J. Am. Chem. Soc.* **1984**, *106*, 6647–6653.

[39] Y. Liu, M. Li, Q. Zhao, H. Wu, K. Huang, F. Li, *Inorg. Chem.* **2011**, *50*, 5969–5977.

[40] J. Torres, M. C. Carrión, J. Leal, F. A. Jalón, J. V. Cuevas, A. M. Rodríguez, G. Castañeda, B. R. Manzano, *Inorg. Chem.* **2018**, *57*, 970–984.

[41] E. Baranoff, B. F. E. Curchod, J. Frey, R. Scopelliti, F. Kessler, I. Tavernelli, U. Rothlisberger, M. Grätzel, M. K. Nazeeruddin, *Inorg. Chem.* **2012**, *51*, 215–224.

[42] K. S. Bejoymohandas, T. M. George, S. Bhattacharya, S. Natarajan, M. L. P. Reddy, *J. Mater. Chem. C* **2014**, *2*, 515–523.

[43] H. Sun, S. Liu, W. Lin, K. Y. Zhang, W. Lv, X. Huang, F. Huo, H. Yang, G. Jenkins, Q. Zhao, et al., *Nat. Commun.* **2014**, *5*, 3601.

[44] G. E. Schneider, H. J. Bolink, E. C. Constable, C. D. Ertl, C. E. Housecroft, A. Pertegás, J. A. Zampese, A. Kanitz, F. Kessler, S. B. Meier, *Dalton Trans.* **2014**, *43*, 1961–1964.

[45] A. Maity, L. Q. Le, Z. Zhu, J. Bao, T. S. Teets, *Inorg. Chem.* **2016**, *55*, 2299–2308.

[46] E. Baranoff, B. F. E. Curchod, *Dalton Trans.* **2015**, *44*, 8318–8329.

[47] W. Lin, Q. Zhao, H. Sun, K. Y. Zhang, H. Yang, Q. Yu, X. Zhou, S. Guo, S. Liu, W. Huang, *Adv. Opt. Mater.* **2015**, *3*, 368–375.

[48] H. Cao, H. Sun, Y. Yin, X. Wen, G. Shan, Z. Su, R. Zhong, W. Xie, P. Li, D. Zhu, *J. Mater. Chem. C* **2014**, *2*, 2150–2159.

[49] G. E. Schneider, A. Pertegás, E. C. Constable, C. E. Housecroft, N. Hostettler, C. D. Morris, J. A. Zampese, H. J. Bolink, J. M. Junquera-Hernández, E. Ortí, M. Sessolo, *J. Mater. Chem. C* **2014**, *2*, 7047–7055.

[50] S. Meng, I. Jung, J. Feng, R. Scopelliti, D. Di Censo, M. Grätzel, M. K. Nazeeruddin, E. Baranoff, *Eur. J. Inorg. Chem.* **2012**, *2012*, 3209–3215.

[51] D. Quiñonero, A. Frontera, D. Escudero, P. Ballester, A. Costa, P. M. Deyà, *Theor. Chem. Acc.* **2008**, *120*, 385–393.

[52] K. Y. Zhang, K. K.-W. Lo, *Inorg. Chem.* **2009**, *48*, 6011–6025.

[53] K. Y. Zhang, S. P.-Y. Li, N. Zhu, I. W.-S. Or, M. S.-H. Cheung, Y.-W. Lam, K. K.-W. Lo, *Inorg. Chem.* **2010**, *49*, 2530–2540.

[54] Y. Hisamatsu, S. Aoki, *Eur. J. Inorg. Chem.* **2011**, *2011*, 5360–5369.

[55] A. M. Bünzli, E. C. Constable, C. E. Housecroft, A. Prescimone, J. A. Zampese, G. Longo, L. Gil-Escrig, A. Pertegás, E. Ortí, H. J. Bolink, *Chem. Sci.* **2015**, *6*, 2843–2852.

[56] C. D. Sunesh, Y. Choe, *Mater. Chem. Phys.* **2015**, *156*, 206–213.

[57] S. Takizawa, R. Aboshi, S. Murata, *Photochem. Photobiol. Sci.* **2011**, *10*, 895–903.

[58] R. D. Costa, E. Ortí, H. J. Bolink, S. Graber, S. Schaffner, M. Neuburger, C. E. Housecroft, E. C. Constable, *Adv. Funct. Mater.* **2009**, *19*, 3456–3463.

[59] F. De Angelis, S. Fantacci, N. Evans, C. Klein, S. M. Zakeeruddin, J.-E. Moser, K. Kalyanasundaram, H. J. Bolink, M. Grätzel, M. K. Nazeeruddin, *Inorg. Chem.* **2007**, *46*, 5989–6001.

[60] D. Tordera, M. Delgado, E. Ortí, H. J. Bolink, J. Frey, M. K. Nazeeruddin, E. Baranoff, *Chem. Mater.* **2012**, *24*, 1896–1903.

[61] A. B. Tamayo, S. Garon, T. Sajoto, P. I. Djurovich, I. M. Tsyba, R. Bau, M. E. Thompson, *Inorg. Chem.* **2005**, *44*, 8723–8732.

[62] J. Sun, F. Zhong, J. Zhao, *Dalt. Trans.* **2013**, *42*, 9595–9605.

[63] L. Benov, *Med. Princ. Pract.* **2015**, *24*, 14–28.

[64] T. J. Jensen, M. G. H. Vicente, R. Luguya, J. Norton, F. R. Fronczek, K. M. Smith, *J. Photochem. Photobiol. B Biol.* **2010**, *100*, 100–111.

[65] T. L. Lam, J. Lai, R. R. Annapureddy, M. Xue, C. Yang, Y. Guan, P. Zhou, S. L.-F. Chan, *Inorg. Chem.* **2017**, *56*, 10835–10839.

[66] N. Iqbal, S. Choi, Y. You, E. J. Cho, *Tetrahedron Lett.* **2013**, *54*, 6222–6225.

[67] R. Gao, D. G. Ho, B. Hernández, M. Selke, D. Murphy, P. I. Djurovich, M. E.

Thompson, *J. Am. Chem. Soc.* **2002**, *124*, 14828–14829.

[68] A. Nakagawa, Y. Hisamatsu, S. Moromizato, M. Kohno, S. Aoki, *Inorg. Chem.* **2014**, *53*, 409–422.

[69] G. R. Fulmer, A. J. M. Miller, N. H. Sherden, H. E. Gottlieb, A. Nudelman, B. M. Stoltz, J. E. Bercaw, K. I. Goldberg, *Organometallics* **2010**, *29*, 2176–2179.

[70] B. N. Axs, *SAINT Area-Detector Integr. Program. SAINT+ v7.12a.; Madison, Wisconsin, USA* **2004**.

[71] G. M. Sheldrick, *SADABS A Progr. Empir. Absorpt. Correct. Version 2004/1; Univ. Göttingen, Göttingen, Ger.* **2004**.

[72] B.-N. Axs, *SHELXTL-NT Struct. Determ. Packag. Version 6.12.; Madison, Wisconsin, USA* **2001**.

[73] M. S. Lowry, W. R. Hudson, R. A. Pascal, S. Bernhard, *J. Am. Chem. Soc.* **2004**, *126*, 14129–14135.

[74] C. A. Parker, *Measurement of Fluorescence Efficiency*, Elsevier Publishing Co., New York, **1968**.

[75] Gaussian 09, Revision D.01, M. J. Frisch, G. W. Trucks, H. B. Schlegel, G. E. Scuseria, M. A. Robb, J. R. Cheeseman, G. Scalmani, V. Barone, B. Mennucci, G. A. Petersson, H. Nakatsuji, M. Caricato, X. Li, H. P. Hratchian, A. F. Izmaylov, J. Bloino, G. Zheng, J. L. Sonnenberg, M. Hada, M. Ehara, K. Toyota, R. Fukuda, J. Hasegawa, M. Ishida, T. Nakajima, Y. Honda, O. Kitao, H. Nakai, T. Vreven, J. A. Montgomery, Jr. , J. E. Peralta, F. Ogliaro, M. Bearpark, J. J. Heyd, E. Brothers, K. Raghavachari, A. Rendell, J. C. Burant, S. S. Iyengar, J. Tomasi, M. Cossi, N. Rega, J. M. Millam, M. Klene, J. E. Knox, J. B. Cross, V. Bakken, C. Adamo, J. Jaramillo, R. Gomperts, R. E. Stratmann, O. Yazyev, A. J. Austin, R. Cammi, C. Pomelli, J. W. Ochterski, R. L. Martin, K. Morokuma, V. G. Zakrzewski, G. A. Voth, P. Salvador, J. J. Dannenberg, S. Dapprich, A. D. Daniels, O. Farkas, J. B. Foresman, J. V. Ortiz, J. Cioslowski, D. J. Fox, Gaussian, Inc. Wallingford CT, **2013**.

[76] A. D. Becke, *J. Chem. Phys.* **1993**, *98*, 5648–5652.

[77] C. T. Lee, W. T. Yang, R. G. Parr, *Phys. Rev. B* **1988**, *37*, 785–789.

[78] M. M. Francl, *J. Chem. Phys.* **1982**, *77*, 3654.

[79] P. C. Hariharan, J. A. Pople, *Theor. Chim. Acta* **1973**, *28*, 213–222.

[80] P. J. Hay, W. R. Wadt, *J. Chem. Phys.* **1985**, *82*, 299.

[81] G. Scalmani, M. J. Frisch, *J. Chem. Phys.* **2010**, *132*, 114110.

[82] A. V Marenich, C. J. Cramer, D. G. Truhlar, *J. Phys. Chem. B* **2009**, *113*, 6378–6396.

[83] J. A. Howard, G. D. Mendenhall, *Can. J. Chem.* **1975**, *53*, 2199–2201.